UNIVERSITY OF TARTU
Faculty of Science and Technology
Institute of Physics

Hanna Liis Tamm

Observational properties of hot spots around relativistic fluid spheres

Bachelor's Thesis (12 ECTS)

Supervisors: João Luís Rosa, PhD
Laur Järv, PhD

Tartu 2023

Observational properties of hot spots around relativistic fluid spheres

Abstract:

With the increasing precision of instruments detecting phenomena close to the event horizon of black holes (BHs), the possibility of new visual signatures can be investigated, testing the evidence for BH mimickers. In this work, we analyze the visual properties of infra-red radiation sources e.g. hot spots around relativistic constant density fluid stars supported by a thin shell. We consider configurations of the fluid star without a thin shell, with and without light rings (LRs). With a supplementary analysis focused on finding the radii of LRs for various configurations, we produce astrometric data via simulations in the GYOTO software. Our results imply qualitative differences in the visual signatures of the hot spot – we find configurations, which resemble either classic BHs, non-ultra compact horizonless compact objects or ultra-compact horizonless objects. Thus, we have found observational properties, which validate the fluid star model as a BH mimicker, as well as qualitative differences, which could be used to distinguish the compact object from a classic BH. By the next generation of experiments in gravitational physics, this distinction might become possible.

Keywords: black hole mimicker, hot spot, thin-shell formalism.

CERCS: P190 - Mathematical and general theoretical physics, classical mechanics, quantum mechanics, relativity, gravitation, statistical physics, thermodynamics.

Kuumkohtade signaalid relativistliku voolisega modelleeritud tähtede ümber

Lühikokkuvõte:

Tänu hiljutistele arengutele interferomeetria valdkonnas on gravitatsiooniga seotud nähtusi võimalik uurida mustade aukude sündmuste horisondile aina lähemal. Tänu sellele tekib võimalus tuvastada signaale, mis erinevad klassikalisete käsitluste ennustustest ning seega vihjavad mustade aukude jäljendajate olemasolule. Selles töös uuriti infrapunakiirguse allikate ehk kuumkohtade visuaalseid signaale tähtede lähedal, mille mateeriat kirjeldab õhukese piirpinnaga ümbritsetud konstantse tihedusega voolis. Töös uuriti mudeli erinevaid variante ilma piirpinnata ning sõltuvalt variandist erineva arvu valgusrõngastega. Lisaks analüütilisele osale, kus leiti valgusrõngaste olemasolu ning nende raadiused sõltuvalt mudelist, simuleeriti mudelit GYOTO tarkvara abil ning loodi astromeetrilised andmed. Saadud tulemused vihjavad kvalitatiivsetele erinevustele – leiti erinevad variandid mudelist, mis sõltuvalt tähe raadiusest jäljendavad kas klassikalist musta auku, horisondita kompaktset objekti ilma valgusrõngasteta või horisondita kompaktset objekti valgusrõngastega. Seega leiti kuumkohtade visuaalsed omadused, mis tõestavad antud mudeli õigsust musta augu jäljendajana ning lisaks leiti uued kvalitatiivsed omadused, mis võimaldavad antud objekti mustast augist eristada.

Võtmesõnad: musta augu jäljendaja, kuumkoht, õhukese kihi formalism.

CERCS: P190 - Matemaatiline ja üldine teoreetiline füüsika, klassikaline mehaanika, kvantmehaanika, relatiivsus, gravitatsioon, statistiline füüsika, termodünaamika.

Contents

Introduction

Black holes (BHs) are extremely dense astrophysical objects characterized by strong gravitational fields, which can even warp the trajectories of photons into circular orbits. The study of BHs in modern physics has much significance, proven in part by recent achievements regarding the detection of gravitational waves [1–4] and the first ever image of a black hole shadow [5–8]. BH models are widely recognized in GR for multiple reasons. The singularity – a conjectural result in the mathematical description of BHs which predicts infinite energy density – is hidden behind the event horizon and causally disconnected from the observer, therefore having no discernible effects further than the event horizon [9]. So far, there have been no observations indicating the existence of other BH-like objects. Yet, as detection methods improve, one can investigate gravitational effects closer to the event horizon than before and therefore aid us in resolving various issues encountered in BH models.

According to Penrose's weak cosmic censorship conjecture, singularities will always be hidden from the outside observer [9]. However, as of yet there is no proof that the field equations corresponding to BHs always evolve regular initial data towards regular final states [10]. Another significant issue rises from the no-hair theorem, stating that all isolated BHs can be fully described by their mass and angular momentum [11]. Information about infalling bodies is radiated from the BH in the form of Hawking radiation, which only carries information about the mass, angular momentum and charge of the initial state [12]. As all other features are lost, the initial state of the BH cannot be recalled, resulting in the information loss paradox. In addition, the currently most accepted cosmological model cannot yet explain the nature of dark matter [13]. Testing the classical BH model is not only for the purpose of scrutiny, but it is also necessary to define the limits of what can be observed in testing event horizons.

BH models and their features describing gravitational interaction are not yet fully understood and therefore deserve some revision. To explain dark matter, new fundamental fields are constructed, which comprise of exotic particles such as axions [14] and other axion-like particles [15]. The simplest theory describes boson stars – self-gravitating fundamental fields made of matter whose interaction with normal matter – Standard Model particles – is weak [16]. Other BH mimickers include fluid stars [17] and gravastars [18]. Under certain conditions, these exotic compact objects (ECOs) are indistinguishable from BHs with the advantage of having neither event horizons nor singularities [19].

One suitable candidate for a black hole mimicker is a relativistic perfect-fluid star [20]. This compact object can be described by a Schwarzschild constant density star solution (or Schwarzschild interior solution), which is identical to a BH on the exterior, but contains no singularities and no event horizons in the interior [21]. Another suitable candidate is a constant density relativistic perfect-fluid sphere supported by thin shell configurations [22], which consists of an extension of the Schwarzschild star model and could have a compactness arbitrarily close to the compactness of a BH. The model consists of two parts interconnected by a thin shell – an exterior part identical to a non-rotating BH and defined by the exterior Schwarzschild solution; and an interior part describing a non-rotating fluid star, defined by the Schwarzschild interior solution. It has been shown that for certain combinations of parameters both the weak and strong energy conditions are satisfied, the solutions are stable against linear perturbations and therefore the model is suitable for describing alternatives to the BH hypothesis.

Simulating these models paves the way for more complex configurations, including gravastars. Gravastars are described by multi-part models, the simplest of which consists of a de Sitter core and a Schwarzschild exterior part connected by a thin shell [18]. Additional more advanced models include fluid stars with anisotropic pressure [23] and a two-fluid compact star [24].

Recently, the GRAVITY instrument of the European Space Observatory has detected near-infrared signals originating from the center of the Milky Way [25]. These flares originate from localised emitting sources called hot spots, which are created by magnetic reconnection events in the accretion flow around a BH [26]. This phenomenon is thought to take place very close to the innermost stable circular orbit [25, 27], describing the interaction of matter and gravity near the event horizon. In models without horizons, the movement of photons is not restricted, therefore the observational signatures of hot spots around these ECOs differ from the signatures of hot spots around BHs [28]. Analyzing the motion of hot spots around compact objects provides deeper insight into strong gravitational fields and could potentially serve as a tool to distinguish compact objects from each other.

In this thesis, the orbits of hot spots around fluid stars and thin-shell fluid stars are simulated using the ray-tracing software Gyoto [29]. In order to simulate the chosen object, the source code is modified via the addition of a plug-in which is used to define a new metric as a piecewise function. Astrometric data, produced with Python scripts, consists of time integrated images, total temporal fluxes, temporal magnitudes and temporal centroids, and can be directly compared with observational data. In addition, the mechanics of the star – the effective potential governing the stability of orbits – is analyzed for different star configurations with the aid of Mathematica.

The thesis is divided into three main sections. Section 1 provides a theoretical background into the theory of fluid stars, including an analysis focused on the thin shell fluid model in Section 1.4. Section 2 gives an overview of the implementation of the fluid star model in the GYOTO software. The results of the simulations, including astrometric observables are analyzed in Section 3.

1 Theory of fluid stars

The aim of this chapter is to provide the necessary framework to describe various fluid star models. Section 1.1 intends to introduce basic concepts, mathematical definitions and conventions used in GR. In Section 1.2, the structure of spherically symmetric compact objects is described. Section 1.3 describes perfect fluid star and thin shell fluid star models. The analysis of LRs for fluid star models is given in section 1.4 and finally, Section 1.5 provides insight into the visual signatures of hot spots.

1.1 Introduction to general relativity

To simplify the forms of equations, geometrical units are employed henceforth, where Newton's gravitational constant G and the speed of light c are set to unity, $G = c = 1$. Equations which include the use of superscripts or subscripts as Greek letters signify tensor equations and employ the conventions of Einstein summation. The corresponding indices (i.e. μ, ν, α, β) take on values $0, 1, 2, 3$. The metric signature used in this thesis is $-, +, +, +$. This section is based on [30], [31], unless stated otherwise.

In order to describe any astrophysical object, one needs to first specify the coordinates and the framework. In GR, the framework is represented by a spacetime – a four-dimensional mathematical structure consisting of three space components and one time component. Any point in the spacetime can therefore be described by four coordinates, which can be written compactly as a four-dimensional vector $x^\mu = (ct, x, y, z)$, where t is the time coordinate and x, y, z space coordinates. Multiplicating the time coordinate by c is required to ensure that all the components have the same units.

General relativity is an example of a field theory. Similarly to classical mechanics, the theory is constructed using Lagrangian formalism, formulating the principle of least action: the action functional S, an integral of the Lagrangian function, which is a function of generalized coordinates and velocities, must remain stationary under small perturbations. The principle of least action forms the basis for the Einstein field equations (EFE), describing the curvature of spacetime caused by the presence of matter:

$$G_{\mu\nu} + \Lambda g_{\mu\nu} = 8\pi T_{\mu\nu},$$

where $G_{\mu\nu}$ is the Einstein tensor, Λ is the cosmological constant, $g_{\mu\nu}$ is the metric tensor and $T_{\mu\nu}$ is the energy momentum tensor. The solutions to these equations form the elements of the metric $g_{\mu\nu}$, which describes the geometry of the spacetime. The metric is related to the line element ds^2 in the form of

$$ds^2 = g_{\mu\nu} dx^\mu dx^\nu,$$

where dx^μ, dx^ν are components of the differential (cdt, dx, dy, dz). For example, the line element of a flat, Minkowski spacetime can be written as

$$ds^2 = -c^2 dt^2 + dx^2 + dy^2 + dz^2.$$

Thus, the line element can be interpreted as distance in the four-dimensional space. As can be seen from the previous definition, the metric in the Minkowski spacetime is

$$g_{\mu\nu} = \begin{pmatrix} -1 & 0 & 0 & 0 \\ 0 & 1 & 0 & 0 \\ 0 & 0 & 1 & 0 \\ 0 & 0 & 0 & 1 \end{pmatrix}$$

and the components of space and time have opposite signs, marked by the metric signature $-,+,+,+$.

In general field theory, the Lagrangian density $\mathcal{L}$ is used, which is a function of the metric $g_{\mu\nu}$ and the covariant derivatives of the vector x^μ with respect to the proper time τ [32]. The action functional of a relativistic point particle is thus expressed as

$$S = \int d\lambda\, 2\mathcal{L} = \int d\lambda \left(g_{\mu\nu} \frac{dx^\mu}{d\tau} \frac{dx^\nu}{d\tau} \right).$$

Using the principle of least action, the Euler-Lagrange equations in the form

$$\frac{d}{d\tau}\left(\frac{\partial \mathcal{L}}{\partial \dot{x}^i}\right) - \frac{\partial \mathcal{L}}{\partial x^i} = 0 \tag{1}$$

can be derived, producing the equations of motion.

To describe the change in coordinates for a basis change (for example, from Cartesian coordinates to curvilinear coordinates), the Christoffel symbols (of the second kind) are introduced, calculated from the metric as

$$\Gamma^\alpha{}_{\gamma\beta} = \frac{1}{2} g^{\alpha\mu}(g_{\mu\beta,\gamma} + g_{\mu\gamma,\beta} - g_{\beta\gamma,\mu}),$$

where the indices after commas denote partial derivatives.

1.2 Spherically symmetric solutions

Note that this section is based on [31, 32], unless specified otherwise.

Calculating the metric and Christoffel symbols for each metric separately proves to be an arduous process, therefore it is useful to generalize. Spherically symmetric spacetimes such as those of BHs and spherical stars are most conveniently described with the aid of spherical coordinates $x^\mu = (ct, r, \theta, \phi)$, with a differential $dx^\mu = (c\,dt, dr, d\theta, d\phi)$. In static spherically symmetric spacetimes, the line element takes the general form

$$ds^2 = -f(r)dt^2 + g(r)^{-1}dr^2 + r^2 d\Omega^2, \quad \text{or} \quad ds^2 = g_{tt}\, dt^2 + g_{rr}\, dr^2 + r^2 d\Omega^2 \tag{2}$$

where $d\Omega^2 = d\theta^2 + \sin^2\theta d\phi^2$ and $f(r) = -g_{tt}$, $g(r) = g_{rr}^{-1}$ are functions specific to spacetimes. For example, the Schwarzschild spacetime describing a spherically symmetric non-rotating electrically neutral BH is given by

$$f(r) = g(r) = 1 - \frac{2M}{r}, \tag{3}$$

where M is the total mass of the spacetime. Birkhoff's theorem states that any spherically symmetric solution of the Einstein field equations will have an exterior metric described by the Schwarzschild exterior solution (3).

In some cases (i.e. the Schwarzschild case), the spacetime gives rise to noteworthy features such as the singularity and the event horizon. As can be seen from Eqs. (2-3), the metric components of the Schwarzschild solution g_{tt} diverges at $r = 0M$ and vanishes at $r = 2M$; g_{rr} diverges at $r = 2M$ and vanishes at $r = 0M$. The Kretschmann scalar $R^{\mu\nu\rho\sigma}R_{\mu\nu\rho\sigma}$ which is related to the curvature of the spacetime becomes infinite, which implies a singularity in the spacetime. As opposed to $r = 0M$, the coordinate singularity at $r = 2M$ does not imply a divergence in the curvature and is therefore a result of the choice of the coordinate system. The event horizon encompasses a region of spacetime from which light cannot escape. In more rigorous terms, the event horizon is a hypersurface separating two regions - the exterior containing spacetime points connected to infinity by timelike paths (where $ds^2 < 0$) and the interior containing points with no such property. For Schwarzschild BHs, the event horizon stands at a radial distance $r = 2M$.

The visual signatures of compact objects depend on the motion of timelike particles (particles with mass) and null particles (particles without mass, i.e. photons). Similarly to classical mechanics, the qualitative features of geodesic motion can be derived from the Lagrangian

$$2\mathcal{L} = g_{\mu\nu}\dot{x}^\mu \dot{x}^\nu = -f(r)\dot{t}^2 + g(r)^{-1}\dot{r}^2 + r^2(\dot{\theta}^2 + \sin^2\theta\,\dot{\phi}^2]) \tag{4}$$

In Hamiltonian mechanics, the canonical momenta p^i associated with a given coordinate x^i are defined as the derivatives of the Lagrangian with respect to $\dot{x}^i$ (the derivative of the coordinate with respect to the proper time). Thus, the momenta are as follows:

$$\begin{aligned} p_t &= \frac{\partial \mathcal{L}}{\partial \dot{t}} = -f(r)\dot{t}, \\ p_r &= \frac{\partial \mathcal{L}}{\partial \dot{r}} = g(r)^{-1}\dot{r}, \\ p_\theta &= \frac{\partial \mathcal{L}}{\partial \dot{\theta}} = r^2\dot{\theta}, \\ p_\phi &= \frac{\partial \mathcal{L}}{\partial \dot{\phi}} = r^2\sin^2\theta\dot{\phi}. \end{aligned}$$

The Hamiltonian $\mathcal{H} = p_\mu \dot{x}^\mu - \mathcal{L}$ coincides with the Lagrangian $\mathcal{H} = \mathcal{L}$, allowing us to define a constant $\delta = -2\mathcal{L}$. Since the Lagrangian defined in Eq. (4) does not depend explicitly on the coordinates t and ϕ, the Euler-Lagrange equations show that the canonical momenta associated with these coordinates will be conserved. These two conserved quantities are defined as the energy $E = p_t = -f(r)\dot{t}$ and angular momentum $L = p_\phi = r^2\sin^2\theta\dot{\phi}$. In a spherically symmetric spacetime, one can restrict the movement to the equatorial plane $\theta = \pi/2$ without loss of generality, thus allowing for the simplification $\sin^2\theta = 1$ and $L = r^2\dot{\phi}$.

Substituting the energy and angular momentum into the Lagrangian (4) and setting $\sin^2\theta = 1$, $\dot{\theta} = \ddot{\theta} = 0$ for the equatorial plane, one finds that

$$\delta = -2\mathcal{L} = f(r)\frac{E^2}{f(r)^2} - \frac{\dot{r}^2}{g(r)} - r^2\frac{L^2}{r^4} = \frac{E^2}{f(r)} - \frac{\dot{r}^2}{g(r)} - \frac{L^2}{r^2}.$$

Solving for $\dot{r}^2$ allows one to find the effective potential defined as

$$\dot{r}^2 = V(r) = g(r)\left(\frac{E^2}{f(r)} - \frac{L^2}{r^2} - \delta\right), \tag{5}$$

where δ is a constant parameter distinguishing massless ($\delta = 0$) and massive ($\delta = 1$) particles. Using the potential, one can infer the stability of the orbits via its derivatives with respect to the radial coordinate $V'(r), V''(r)$. Stable orbits are possible in regions where the potential obeys the relation $V''(r) < 0$, in all other cases, the orbit will be unstable.

By setting $\dot{r} = \ddot{r} = 0$, one can analyze circular orbits and their stability. In Schwarzschild spacetimes, circular trajectories for massive particles, i.e., $\delta = 1$, are only stable when $r \geq 6M$, the orbit $r = 6M$ defining the innermost stable circular orbit (ISCO). The angular frequency of the circular orbit measured at infinity can be calculated from the following equation:

$$\Omega_C^2 = \frac{f'(r)}{2r} \tag{6}$$

The set of all circular orbits of null particles (circular null geodesics) and its slice are respectively defined as the photon sphere and LR. In the Schwarzschild spacetime (3), there exists only one unstable LR, which stands at $r = 3M$ [33].

Incoming photons with varying energy and angular momentum will behave differently. This type of behaviour is described by the impact parameter $b = L/E$ - photons with a high impact parameter will be slightly deflected, while photons with a small impact parameter will be absorbed. For Schwarzschild BHs, this parameter is equal to

$$b = \frac{L}{E} = \frac{r\sqrt{Mr}}{r - 2M}.$$

The limit defining the transition between absorption and deflection is the critical impact parameter, which corresponds to photons asymptotically approaching the LR. In the Schwarzschild spacetime, one can find the limit by approaching the LR at $r \to 3M$, thus the critical impact parameter is $b_c = 3\sqrt{3}M$. This defines the radius of the shadow - the visual boundary of the dark region surrounding the compact object.

1.3 Perfect fluid stars and thin shell configurations

This section is based on [22], unless specified otherwise.

A non-rotating star of incompressible isotropic perfect fluid can be described in two parts, matched together at a radial distance of R, equal to the radius of the star. The interior is described by the Schwarzschild interior solution and the exterior by the Schwarzshild exterior solution, the latter of which is identical to a BH. The Schwarschild interior solution ($r < R$) is represented by the line element for which the functions $f(r)$ and $g(r)$ are

$$f(r) = -\frac{1}{4}\left(3\sqrt{1 - \frac{2M}{R}} - \sqrt{1 - \frac{2r^2M}{R^3}}\right)^2, \tag{7}$$

$$g(r) = \left(1 - \frac{2r^2M}{R^3}\right)^{-1}, \tag{8}$$

and the exterior solution ($r > R$) is described by (3).

According to Buchdal's theorem, if the radius of a relativistic fluid sphere with constant density R is smaller than $9M/4$, where M is the total mass of the star, the central pressure becomes infinite and a singularity appears in the center [34]. Therefore, for physically relevant solutions, one needs to look at configurations where $r \geq 9M/4$.

The central pressure p_c or the pressure at the center of the fluid star is equal to

$$p_c = p(0) = \rho\frac{1 - \sqrt{1 - \frac{2M}{R}}}{3\sqrt{1 - \frac{2M}{R}} - 1}, \tag{9}$$

where the energy density ρ is a constant. If $R = R_b$, we find from Eq. (7) that the metric component $g_{tt} = 0$, which corresponds to a coordinate singularity. Taking the limit $R \to R_b$ of Eq. (9) implies the divergence of the central pressure, which implies that the coordinate singularity in g_{tt} corresponds to a curvature singularity in the Ricci scalar $R = R^\alpha{}_\alpha$. We can describe this phenomena with the term singularity, but it is important to note that this is not an identical case with the Schwarzschild BH singularity.

The Buchdahl theorem specifies the solutions that are physically relevant, therefore setting an apparent lower limit on the radius of the star. The theorem is based on the following assumptions:

1. GR is a valid theory of gravity;
2. The solution is spherically symmetric;
3. The star consists of a single, perfect fluid;
4. The fluid is isotropic or slightly anisotropic (in cases where the tangential pressure is slightly smaller than the radial pressure);
5. The radial pressure and energy density are non-negative;
6. The energy density is a non-increasing function of the radial distance increases.

But, by discarding one or more of the assumptions, one could bypass the Buchdahl limit and obtain a relevant solution for an ECO with a larger compacticity.

In the process of constructing more complex models of ECOs, one also needs to take into account the energy conditions - the weak energy condition (WEC) states that the average energy density as measured by any timelike observer must be strictly positive and the strong energy condition (SEC) formulates that the trace of the tidal tensor must be non-negative, which preserves the attractive character of gravity. In addition, the dominant energy condition (DEC) stipulates nothing can move faster than the speed of light - matter should flow along timelike or null world lines. While these energy conditions can be violated (for example, the Casimir effect [35]), their validity strongly supports the physical relevance of ECO models.

Choosing a star radius greater than the Buchdahl limit $R > R_b = 9M/4$, a more complex model can be constructed, which similarly to a fluid star consists of two parts. Contrary to the fluid star model, the two parts are not connected at a distance equal to the radius of the star, but rather a different radius R_s. At that distance, an infinitesimally thin shell is formed, which has a mass equal to the mass of the exterior layers of the star, as if the layers were compressed into a shell. The shell is described by the line element

$$ds^2 = -d\tau^2 + R_s^2(d\theta^2 + \sin^2\theta\, d\phi^2), \tag{10}$$

where τ denotes the proper time coordinate and R_s is defined as the radius of the shell - the radial distance at which the transition between spacetimes occurs. To properly describe the two-part model, one needs to confirm that the union of two metrics still form a valid solution to the Einstein field equations.

First, a more rigorous description of the situation is required: a hypersurface Σ separates spacetime into two regions: the interior $\mathcal{V}^-$ described by the metric $g^-_{\alpha\beta}$ and the exterior $\mathcal{V}^+$ described by $g^+_{\alpha\beta}$. The joined metric $g_{\alpha\beta}$ is expressed by the interior metric $g^-_{\alpha\beta}$ and exterior metric $g^+_{\alpha\beta}$ as

$$g_{\alpha\beta} = \Theta(l)g^+_{\alpha\beta} + \Theta(-l)g^-_{\alpha\beta}, \tag{11}$$

where $\Theta(l)$ is the Heaviside distribution function of the proper distance l, defined equal to +1 if $l > 0$, 0 if $l < 0$ and indeterminate if $l = 0$. Since the derivative of the Heaviside function with respect to the proper time is equal to the Dirac delta function $\delta(l)$, differentiating the equation and calculating the Christoffel symbols generates terms proportional to $\Theta(l)\delta(l)$. As $\Theta(l)$ is undefined at $l = 0$, these products are undefined. Thus, to eliminate the discrepancies, one needs to impose additional conditions, formulated as the junction conditions. The first junction condition states that the induced metric h_{ab} must be continuous across the hypersurface Σ. The induced metric is the metric defined on the hypersurface Σ and is obtained by restricting the line element ds^2 to the hypersurface Σ – if x^a are the coordinates of the spacetime and y^a the coordinates of the hypersurface, then the line element on the hypersurface relates to the induced metric h_{ab} as follows:

$$ds^2_\Sigma = g_{ab}\, dx^a dx^b = h_{ab}\, dy^a dy^b.$$

Therefore, the first junction condition is in the form

$$[h_{ab}] = 0,$$

where $[h_{ab}] = h_{ab}(\mathcal{V}^+)|_\Sigma - h_{ab}(\mathcal{V}^-)|_\Sigma$ is the jump of h_{ab} across the hypersurface Σ.

For solutions with thin shells, the second junction condition relates the extrinsic curvature K_{ab} to the stress-energy tensor $S_{\alpha\beta}$ of the thin shell in the form

$$S_{ab} = -\frac{1}{8\pi}([K_{ab}] - [K]h_{ab}),$$

where K is the trace of the extrinsic curvature K_{ab}. The extrinsic curvature is a symmetric three-dimensional tensor, which measures the bending of the hypersurface in spacetime and represents the normal component of the vector field tangent to the hypersurface Σ. Following from the junction conditions, one can find the density and pressure of the thin-shell model.

This model has been shown to satisfy the weak and strong energy conditions and could have a compacticity similar to that of a BH. Furthermore, when choosing a shell radius $R_s \gtrsim 2M$, one can obtain a solution without a singularity, thus describing a situation not encompassed by the Buchdahl theorem. In this case, the last assumption of the Buchdahl theorem does not apply, since the density of the thin shell is greater than the density of the star. In particular, since the shell is two-dimensional, the density of the shell is infinite. For certain values of the parameters - the star radius R and shell radius R_s, the solutions are stable against linear radial perturbations; therefore, they serve as viable models for dark matter or ECOs.

In ultracompact spacetimes without singularities and event horizons, such as the one investigated in this thesis, LRs appear in pairs [36]. The behaviour of LRs is analyzed for different shell and star parameters in Section 1.4, with a similar approach as [37].

1.4 Effective potential and light rings

With the introduction of the fluid star model, we can now repeat the analysis ofthe geodesic structure, analyzing the motion of photons around the fluid star. The metric components of the interior and exterior Schwarzschild metric are as follows:

$$g_{tti} = -\frac{1}{4}\left(3\sqrt{1-\frac{2M}{R}} - \sqrt{1-\frac{2r^2M}{R^3}}\right)^2, \qquad g_{tte} = -\left(1-\frac{2M}{r}\right),$$
$$g_{rri} = \left(1-\frac{2r^2M}{R^3}\right)^{-1}, \qquad g_{rre} = \left(1-\frac{2M}{r}\right)^{-1}.$$

These components are then combined into a piecewise metric as defined in Eq. (11):

$$g_{tt} = \Theta(r-R_s)g_{tte} + \Theta(R_s-r)g_{tti},$$
$$g_{rr} = \Theta(r-R_s)g_{rre} + \Theta(R_s-r)g_{rri},$$

ensuring that when $r < R_s$, the metric coincides with the interior solution - $\Theta(r-Rs) = 0$ and $\Theta(R_s - r) = 1$; and when $r > R_s$, the metric is the exterior Schwarzschild metric as $\Theta(r-R_s) = 1$ and $\Theta(R_s - r) = 0$. At the shell radius $r = R_s$, the Heaviside function is

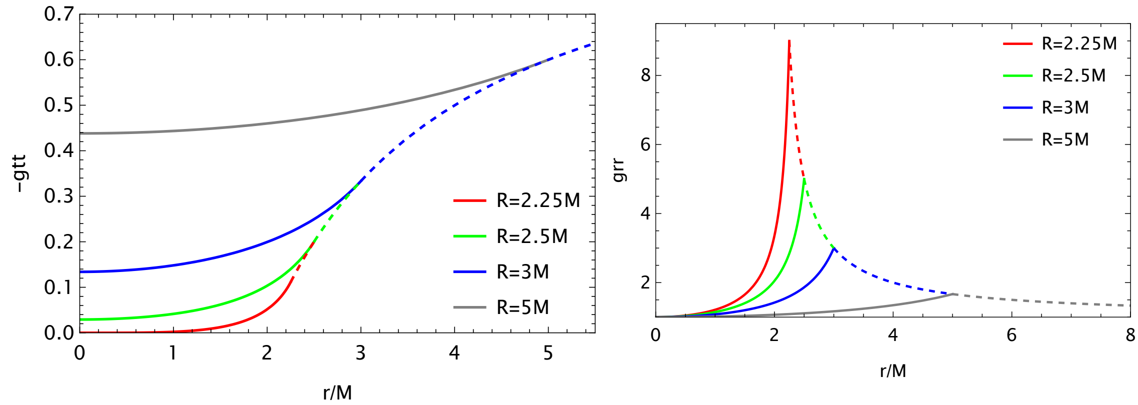

Figure 1. Comparison of the metrics. Left: $-g_{tt}$ component of the metric, right: g_{rr} component of the metric, plotted for various parameters.

indeterminate. This discrepancy can be removed by defining $\Theta(l) = 1$ at $l = 0$. The components of the chosen piecewise metric $g_{tt}(r) = -f(r)$ and $g_{rr}(r) = g(r)^{-1}$ are plotted in Fig. 1. The dashed line represents the exterior Schwarzschild metric and the solid line represents the interior Schwarzschild metric.

Finding the radii of LRs reduces to finding maxima and minima of the potential function $V(r)$. Since the components g_{tti}, g_{rri} of the interior Schwarzschild solution do not change in sign ($g_{tti} < 0$ and $g_{rri} > 0$) and are strictly increasing, multiplying the potential in Eq. (5) with $f(r)/g(r) = -g_{tti}g_{rri}$ does not change the extrema of the potential. Thus, preserving the potential's qualitative features, the potential can be redefined as

$$\bar{V}(r) = \frac{f(r)}{g(r)} V(r) = E^2 - f(r)\frac{L^2}{r^2} = E^2 + g_{tt}\frac{L^2}{r^2}. \tag{12}$$

In the exterior Schwarzschild spacetime and any compact spacetime with an event horizon, the g_{tt} and g_{rr} components change in sign. But, since $f(r) = g(r)$ in the exterior Schwarzschild solution, one can simply write the potential (5) as

$$V(r) = f(r)\left(\frac{E^2}{f(r)} - \frac{L^2}{r^2}\right) = E^2 - f(r)\frac{L^2}{r^2} = E^2 + g_{tt}\frac{L^2}{r^2}$$

and follow a similar procedure.

Circular orbits of photons can be found by setting the potential and its derivative with respect to the radial coordinate equal to zero: $V(r) = V'(r) = 0$. The corresponding set of equations is a system of linear equations for the energy E^2 and the angular momentum L^2. For the purpose of brevity, the solutions for the energy and angular momentum are not shown. As differentiating the Heaviside distribution function produces the Dirac delta function, the condition $V'(r) = 0$ produces an equation dependent on both Θ and δ:

$$\frac{2L^2}{r^3}\left(g_{tte}\Theta(r-R_s) - g_{tti}\Theta(R_s-r)\right) + \frac{L^2}{r^2}\Bigg(g_{tte}\delta(r-R_s) + g_{tti}\delta(R_s-r) -$$
$$\frac{2M}{r^2}\Theta(r-R_s) + Mr\Theta(R_s-r)\left(\frac{1}{R^3} - \frac{3\sqrt{1-\frac{2Mr^2}{R^3}}\sqrt{1-\frac{2M}{R}}}{R^3-2Mr^2}\right)\Bigg) = 0$$

Assuming a non-trivial angular momentum and radius $L^2 \neq 0, r \neq 0$, we obtain

$$2\left(g_{tte}\Theta(r-R_s) - g_{tti}\Theta(R_s-r)\right) + r\left(g_{tte}\delta(r-R_s) + g_{tti}\delta(R_s-r) - \right.$$
$$\left.\frac{2M}{r^2}\Theta(r-R_s) + Mr\Theta(R_s-r)\left(\frac{1}{R^3} - \frac{3\sqrt{1-\frac{2Mr^2}{R^3}}\sqrt{1-\frac{2M}{R}}}{R^3-2Mr^2}\right)\right) = 0$$

Consider the following cases: $r < R_s$, $r = R_s$ and $r > R_s$. The condition $r < R_s$ results in a LR in the interior of the star. In this case, $\Theta(r-R_s) = 0, \Theta(R_s-r) = 1$ and $\delta(r-R_s) = \delta(R_s-r) = 0$ and the equation $V'(r) = 0$ simplifies to the form

$$-2g_{tti} + Mr^2\left(\frac{1}{R^3} - \frac{3\sqrt{1-\frac{2Mr^2}{R^3}}\sqrt{1-\frac{2M}{R}}}{R^3-2Mr^2}\right) = 0,$$

from which we obtain a quadratic equation for r. Discarding the negative solutions, we obtain

$$\begin{aligned} r_{LR1} &= R\sqrt{9-\frac{4R}{M}}, \\ r_{LR2} &= \sqrt{\frac{(9M-4R)R}{(18M-9R)M}}R = R\sqrt{\frac{R}{R_b}}\sqrt{\frac{R-R_b}{R-2M}}, \end{aligned} \tag{13}$$

where $R_b = 2.25M$ is the Buchdahl limit. Note that if $R > R_b$, the first solution r_{LR1} becomes imaginary; if $R = R_b$, then $r_{LR1} = 0$. Since we are interested in physically relevant solutions $R \geq 2.25M$, the first solution r_{LR1} can be discarded and the second solution r_{LR2} can be analyzed based on the assumption $R \geq 2.25M$. The second solution r_{LR2} produces different results dependent on the radius R, where the stability of the LRs can be inferred from the second derivative $V''(r)$.

- If $R = 2.25M$, the single solution satisfying $V'(r) = 0$ is $r = 0M$, which corresponds to a stable potential well in the center of the star. Including the unstable Schwarzschild LR at $r = 3M$, we thus find only the Schwarzschild LR at $r_{LR} = 3M$.
- If $2.25M < R < 3M$, the formula produces a real-valued solution at a radius less than the star radius $r < R$, implying a stable LR in the interior. Thus, we find a pair of LRs: a stable LR at $r < R < 3M$ and the unstable Schwarzschild LR at $r = 3M$.
- If $R = 3M$, the solution coincides with the Schwarzschild LR $r = 3M$, thus producing a degenerate pair of LRs at $r = 3M$ - one stable, one unstable, resulting in a single meta-stable LR.
- If $R > 3M$, a real-valued solution is found at a radius greater than the star radius $r > R$, which contradicts the assumption $r < R_s$ since we assume that the shell lies inside the star $R_s \leq R$. Therefore, no LRs exist when $R > 3M$.

Now inspecting the case $r = R_s$, we find that the equation $V'(r) = 0$ includes terms dependent on $\Theta(0)$, which is undefined. The only solution satisfying this equation is $r = 0M$, which can be discarded. If $r > R_s$, then $\Theta(r-R_s) = 1$, $\Theta(R_s-r) = 0$, $\delta(r-R_s) = \delta(R_s-r) = 0$ and the condition $V'(r)$ simplifies to the form

$$2(r-3M) = 0,$$

implying a single LR coinciding with the Schwarzschild LR $r_{LR} = 3M$. If $R_s > 3M$, the Schwarzschild solution does not apply since the assumption $3M = r_{LR} > R_s$ does not hold.

In order to distinguish the motion of massive and massless particles, the potential can be written as

$$\dot{r}^2 = E^2 - 2\mathcal{V}_\delta(r),$$

where the potential can be expressed separately for massive particles and for photons as follows:

$$\begin{aligned} V_{\text{part}} &= 2\mathcal{V}_{\delta=1}(r) = g_{tt}\left(1 + \frac{L^2}{r^2}\right), \\ V_{\text{phot}} &= \frac{2\mathcal{V}_{\delta=0}(r)}{L^2} = \frac{1}{r^2} g_{tt} \end{aligned} \tag{14}$$

The potential for photons as defined in Eq. (14) for various star radii R is plotted in Fig. 2.

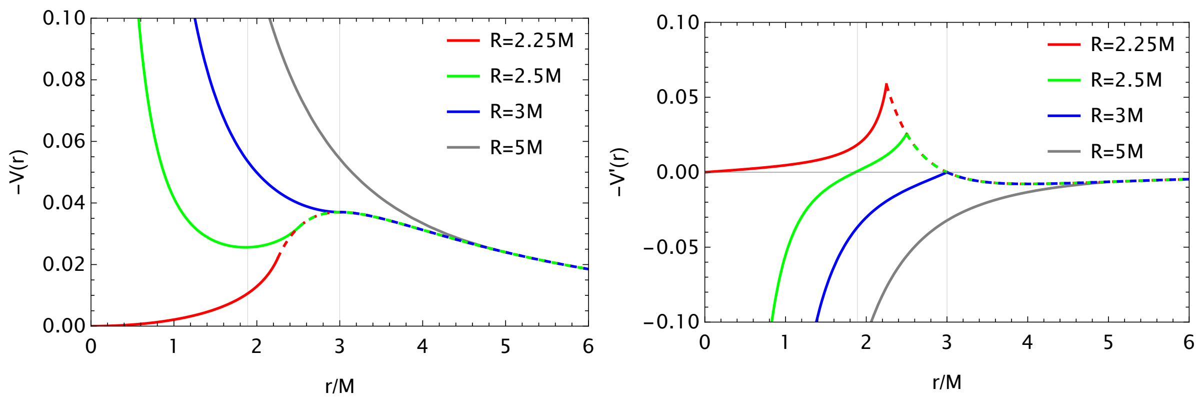

Figure 2. Effective potential $-V_{\text{phot}}(r)$ defined in Eq. (14) (left) and its derivative $-V'_{\text{phot}}(r)$ (right) for photons for fluid stars with radii $R \in \{2.25M, 2.5M, 3M, 5M\}$. The solid line corresponds to the interior solution and the dashed line to the exterior solution. The vertical lines correspond to potential maxima at $\bar{r}_{LR} = 1.89M, r_{LR} = 3M$. Maxima and minima of the potential function indicate the presence of LRs.

The negative sign is chosen for the purpose of illustrating the relation with classical mechanics – a minimum corresponds to a stable orbit and a maximum to an unstable orbit. The potentials for configurations $R \leq 3M$ feature points satisfying $V'(r) = 0$ at $r_{LR} = 3M$, whereas the configuration $R = 5M$ shows none – this is in accordance with obtained results, claiming that at $R > 3M$ no LRs appear. At $2.25M < R < 3M$, a second stable LR appears in the interior of the star in addition to the Schwarzschild LR. The radius of the interior LR increases with the increase in star radius R. At $R = 3M$, the radius of the interior LR is equal to the Schwarzschild LR $\bar{r}_{LR}$, producing an inflection point in the potential and thus a degenerate pair of LRs. As the star radius further increases, no extrema and thus no LRs appear.

The existence of a second LR implies another critical impact parameter corresponding to the stable interior LR, which can be found by taking the limit

$$\bar{b}_c = \lim_{r \to \bar{r}_{LR}} b = \lim_{r \to \bar{r}_{LR}} \frac{L}{E} = \frac{R^2}{\sqrt{M(4R - 9M)}} = \frac{R^2}{2\sqrt{M(R - R_b)}}, \tag{15}$$

where $R_b = 2.25M$ is the Buchdahl limit. Note that this quantity plays no part in our analysis since due to the exterior unstable LR, no photons can asymptotically approach the interior LR. In other words, any incoming photon needs sufficient potential energy to break the potential barrier at $r = 3M$ to reach the interior, but no such photon can stop at the bottom of the potential well. Instead, they are reflected back to the exterior.

For comparison, consider cases where $R \neq R_s$. The potential for various configurations where $R \neq R_s$ is plotted in Fig. 3. In each plot, the shell radius R_s remains constant and radius

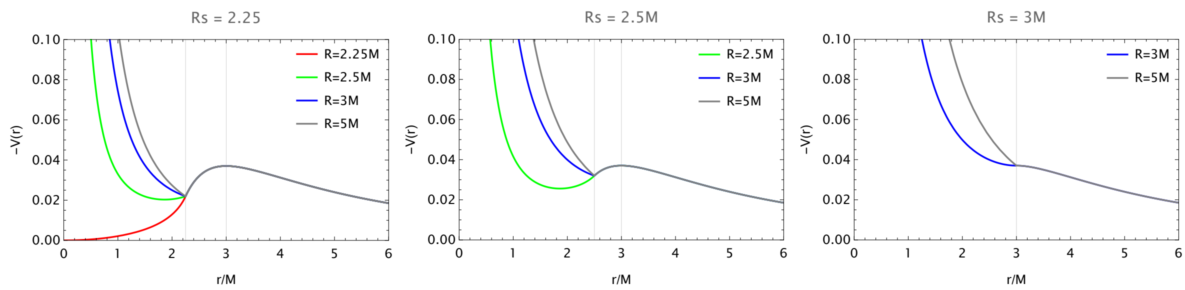

Figure 3. Effective potential $-V_{phot}(r)$ for cases $R_s = const \in \{2.25M, 2.5M, 3M\}$, $R \in \{2.25M, 2.5M, 3M, 5M\}$.

of the star R is a variable. Cases where $R_s > R$ are discarded, since our chosen model requires $R_s < R$. Comparing the potential to cases where $R = R_s$ (see Fig. 2), when the shell lies inside the star, the potential has sharp, non-differentiable points. Due to the drop in potential at the shell radius R_s, new stable LRs form for some configurations ($R = 3M$, $R = 5M$ in the figure on the left; $R = 3M$ in the center figure and $R = 5M$ in the right image in Fig. 3). In one case where a LR already exists - $R = 2.5M$ in the left image, the stable LR increases in stability due to the sharper rise of the potential, making it more difficult for a photon inside the potential well to escape.

1.5 Astrometric observables

Note that this section is based on [28]. Using the metric, the orbital velocity (see Eq. 6) the trajectories of hot spots around ECOs can be calculated. In the ray-tracing software GYOTO, the hot spot is modelled as an isotropically emitting sphere orbiting the compact object in its optically thin accretion disk on the equatorial plane. The program outputs the data as a 2D image, where each pixel represents the specific intensity of the hot spot I^{ν}_{klm} at a given time t_k. The specific intensity is then converted to cubes $I_{klm} = \Delta\nu I^{\nu}_{klm}$, where $\Delta\nu$ is the spectral width. Using the specific intensity, one can produce the following data:

1. time integrated images:

$$\langle I \rangle_{lm} = \sum_k I_{klm}. \tag{16}$$

These images quantify all the pixels that have a non-zero intensity through-out the entire orbit of the hot spot.

2. total temporal fluxes:

$$F_k = \sum_l \sum_m \Delta\Omega I_{klm}.$$

The flux represents the total energy emitted by the hot spot for a given solid angle $\Delta\Omega$ and is used to compute temporal magnitudes.

3. temporal magnitudes

$$m_k = -2.5 \log \left(\frac{F_k}{\min(F_k)} \right). \tag{17}$$

The temporal magnitude is the apparent magnitude of the orbiting hot spot i.e. the brightness of the hot spot as observed from Earth.

4. temporal centroids

$$\vec{c}_k = F_k^{-1} \sum_l \sum_m \Delta\Omega I_{klm} \vec{r}_{lm}, \tag{18}$$

where $\vec{r}_{lm}$ is the position with respect to the centre of the image. The centroid is the weighted average position of all the pixels of the hot spot at a particular spot of the orbital period, at a given solid angle.

Since the GRAVITY instrument is capable of measuring centroids, simulated astrometric data can be directly compared with observational results [25].

In previous works, the time integrated images of hot spots around BHs and boson stars have been investigated. These images feature various components depicted on Fig. 4.

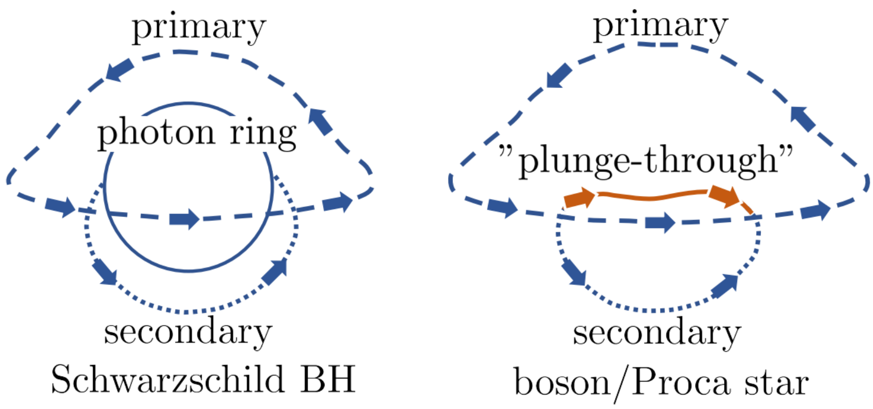

Figure 4. A visual representation of the primary and secondary tracks, the photon ring and the "plunge-through" track around a BH and a boson star. [28]

With the exception of the LR and the "plunge-through" track, the objects feature similar tracks. The primary (top) lensed track represents slightly deflected photons traveling from the source to the observer without crossing the equatorial plane. The secondary (bottom) track corresponds to light crossing the equatorial plane once after emission, by making one half turn around the compact object before reaching the observer. The faint photon ring features photons in a circular orbit and the "plunge-through" track is created by weakly-lensed photons that pass through the compact object. BHs do not feature a "plunge-through" track due to the event horizon and boson stars in this case have no LRs since they are not compact enough. Under certain circumstances, some boson stars produce LRs [38, 39]. Another interesting property which is not visualized in Fig. 4 is that the intensity on the left side of the primary track is greater than on the right side - this property is caused by beaming emission from the approaching left orbit section.

2 Implementation

This chapter gives an overview of the process of implementing a new metric in GYOTO in order to ray-trace the photons and produce the images of the hot spot. The description of the software is based on [29], unless stated otherwise.

2.1 GYOTO

The software GYOTO (General Relativity Orbit Tracer of Observatoire de Paris) is intended for the purpose of producing images of compact objects with some observable astrophysical counterpart, e.g. an orbiting star or accretion disk, via the methods of backwards ray-tracing. While many ray-tracing programs have been developed for the purpose of computing trajectories around compact objects [40, 41], few of them are made public. Thus, the main advantage of GYOTO is its freely available open-source code. Since the code is written in the object-oriented programming language C++, it is easy to modify and implement new models. In addition, GYOTO is capable of implementing more complicated non-analytical metrics. The software solves the equations of motion using the Hamiltonian formalism, which are integrated backwards in time, i.e., starting at the observer and moving towards the system under study. In addition to the initial conditions (the observer's screen and the inclination angle of the photon), the integration is performed with the aid of conserved quantities E and L, as described in Section 1.2. The equations of motion are solved via a Runge-Kutta algorithm of fourth order (RK4), with an adaptive step. Integration continues until one of the stop conditions are fulfilled:

- the photon traced from the observer reaches the emitting source,
- the photon is sufficiently far away from the central object, (note that this condition depends on the astrophysical object)
- the photon approaches an event horizon.

GYOTO can be executed on the command line to ray-trace a single frame, taking inputs from an XML type file and exporting data as a FITS type file. The XML file contains a global field and several sub-fields defining the scene to be ray-traced - for example, the global field `Scenery` and sub-fields `Metric`, `Screen` and `Astrobj`, which respectively describe the scenery, the metric used for the calculations, the properties of the observer's screen such as the distance from the compact object, and the astrophysical object to be ray-traced. The ray-tracing is executed in the code as follows - the function `Scenery::rayTrace` calls `Photon::hit`, which consists of a loop that calls the function `WorldlineIntegState::nextStep` until a stop condition is fulfilled. The function `WorldlineIntegState::nextStep` calls an adaptive RK4 algorithm.

2.2 Implementing the metric

In order to implement the fluid star model consisting of a piecewise metric, a C++ plug-in is added to the software. This is a shared library which contains the initialisation function, the metric, the Christoffel symbols and the orbital velocity for the given metric. The purpose of the initialisation function is to register subcontractors for object classes (such as the metric) via header files so that they can be found by name by other scripts.

The initialisation function is written in the file `InitPlug.C`, located in the directory `plugins/null/lib`. This file takes inputs from a header file (represented by the suffix `.h`, which represents the interface of the metric. Starting the process of implementing the metric, the header file of the metric `GyotoThinShell.h` (see Appendix A.1) is created in the directory `plugins/null/include`, which includes the two free parameters of the metric `par` and `par2`, which respectively represent the radius of the star and the radius of the shell. These are defined in the code via the mutator method – the protected variables are accessed via the accessors and can be modified via the mutators. In the header file, inside the class `Gyoto::Metric::ThinShell`, the parameters are defined as follows:

```
protected:
 double par_ ;  // radius of the star
 double par2_; // radius of the shell

private:

public:
 void par(const double);
 void par2(const double);
 double par() const;
 double par2() const;
```

In addition, the header file defines the structure of the metric components `gmunu`, the Christoffel symbols `christoffel` and the orbital velocity `circularVelocity`. To allow the initialization function access to the header file, the line

```
#include “GyotoThinShell.h”
```

is added to the beginning of the file `InitPlug.C`. In addition, the metric is registered by adding

```
Metric::Register("ThinShell", &Metric::Subcontractor<Metric::ThinShell>);
```

inside the function `__GyotonullInit`. Then, the main metric file `ThinShell.C` (see Appendix A.2) is created in the directory `plugins/null/lib`, which adds the two free parameters and defines the metric components, the Christoffel symbols and the orbital velocity. First, two new properties (radii of the star and the shell) are added:

```
GYOTO_PROPERTY_DOUBLE(ThinShell, Par, par,
                      "Free parameter")     // radius of the star
GYOTO_PROPERTY_DOUBLE(ThinShell, Par2, par2,
                      "Free parameter 2")   // radius of the shell
```

These are included in the constructor, which sets the coordinate kind, the metric kind and the new parameters:

```
ThinShell::ThinShell() :
  Generic(GYOTO_COORDKIND_SPHERICAL, "ThinShell"),
  par_(1),
  par2_(1)
{}
```

The mutators allow one to change these variables:

```
    void ThinShell::par(const double e) {
  par_=e;
  tellListeners();
```

```
}
void ThinShell::par2(const double e) {
  par2_=e;
  tellListeners();
}
```

while the accessors allow access to these protected variables:

```
double ThinShell::par() const { return par_ ; }
double ThinShell::par2() const { return par2_ ; }
```

Then, the metric components, Christoffel symbols and the orbital velocity are defined as separate functions. First, the necessary inputs for calculation are defined as double type variables. As the metric, symbols and the orbital velociry are all piecewise functions, they are defined with an if clause - if the radial coordinate is greater than the radius of the shell, the interior components are chosen and otherwise, the exterior components are chosen. For example, the orbital velocity is calculated as follows:

```
  if (coord[1] > rs) { // Schwarzschild exterior
      vel[3] = 1./((dir*pow(coord[1], 1.5))); // sqrt(1/r^3)
  }
  else { // Schwarzschild interior
      vel[3] = 1./2.*sqrt (a*(-2./R3 + (6.*sqrt (1.-2.*r2/R3)*sqrt
       ↪  ((-2.+R)/R))/(-2.*r2+R3)));
  }
```

Note that whenever $R \neq R_s$, the g_{tt} component of the piecewise metric is discontinuous - thus, to ensure a smooth transition, the interior component g_{tti} is multiplied with a constant $a = g_{tti}/g_{tte}$, calculated at the shell radius R_s.

The plug-in is installed via the `make` utility, which issues commands to recompile new components in the code. The file `Makefile.am` in the directory `plugins/null/lib` is configured to include `ThinShell.C` and the commands `./configure`, `make`, `sudo make install` are run on the command line in the `plugins/null` directory, completing the installation. The metric can be checked with an additional Python script which estimates the Christoffel symbols of the installed metric numerically and compares them to the symbols calculated by the software.

2.3 Python script

An alternative way of providing inputs to the software is via a Python script, which also allows to ray-trace more than a single frame at once. The `interactive_hotspot.py` script (see Appendix A.3) loads the plugin `ThinShell.C` and takes inputs in the form of variables which can be directly inserted into the script. These inputs include the metric, observation angle `obs_angle`, hot spot orbit radius `orbit_radius` and others.

Then, the metric is loaded via the `gyoto.core` Python module. Next, the properties of the system are defined, including the observer's properties, the type of astrophysical object, orbital velocity, properties of the scenery and others. For example, the observation specifications detail the observation angle and the resolution of the screen, among others:

```
obs_theta_deg = obs_angle   # Observation angle in degrees
nt = time_steps                 # Time steps in light curve
Npix = resolution               # Image size in pixels N x N
length = obs_distance           # Times and distances
```

The variables object_type and obj_size are used to define the astrophysical object orbiting the central compact object. The astrophysical object studied in this work - hot spot - is modelled as an isotropically emitting spherical source orbiting around the compact object at a constant orbital radius equal to orbit_radius (in units of M). In the GYOTO interface, this model is defined as a star:

```
if object_type == 2: #star
    equat = gyoto.std.Star()
    equat.radius(obj_size)
    equat.isotropic(True)
```

In order to shorten the simulation time, the script calculates a mask under the if(want_mask) clause by producing an integrated image of the hot spot at all orbital positions and finding the pixels that are illuminated. The mask is created as a clone of the chosen scenery and the pixels which have a non-trivial intensity are saved as an array. The next stage under the if trace_rays clause represents the ray-tracing process. Time is advanced according to the variable number_rays, the position and velocity of the hot spot are updated and the scene is ray-traced according to the previously defined mask and shown as an image. In the case of multiple rays, the ray-tracing is as follows:

```
if trace_rays:
        all_data = np.empty([number_rays, Npix, Npix])
        for i in range(number_rays):
            obs_time = screen_dist_min + i / number_rays * period_min
            screen.time(obs_time,"min")
            equat.setPosition(equat_position)
            equat.setVelocity(equat_velocity)
            # Ray trace the whole image
            if tracing_type == 1:
                image = sceneryEquat.rayTrace()['Intensity']
                all_data[i,:,:] = image
                plt.figure(2)
                plt.imshow(image)
```

The corresponding data cube is saved as a FITS type file, which can be analyzed using the ds9 software.

The script also allows for plotting the geodesics of individual pixels, defined under the if plot_geodesic clause. This requires inputs geod_x, geod_y corresponding with the coordinates of the pixel in the image, which finds the photon associated with the pixel and traces its geodesic until it hits the emitting source. The geodesic of photons is traced in three dimensions and the user can choose on which plane it is projected, using variables such as yz_plot.

In addition, the script can read data from previously saved FITS files and calculate the magnitudes, centroids and integrated flux, as defined in Eqs. (16-18), producing a similar result as [42]. Data from the cube file is extracted into a variable result, which includes the flux and the x and y-positions on each pixel at various orbital positions. For example, the x- and y-coordinates of the centroid are calculated as follows:

```
centroid_x = (result[0,:] - n_pix / 2) * field_view / n_pix
centroid_y = (result[1,:] - n_pix / 2) * field_view / n_pix
```

The magnitudes and centroids are exported as a single TXT file, while the integrated flux is exported as a separate TXT file, representing a heat map.

2.4 Simulation details

The variables shown in Table 1 are kept constant during the simulations. The metric is the

`choose_metric`	2	`screen_dist`	8.25
`spin_par`	0.	`object_type`	2
`metric_mass`	4.26e6	`object_radius`	0.5
`time_steps`	200	`object_thin`	True
`obs_distance`	1000	`mask_radius`	1
`field_view`	200	`number_rays`	180

Table 1. The chosen variables of the Python script `interactive_hotspot.py` for all simulations.

piecewise thin shell metric, on which the spin parameter `spin_par` has no effect and can thus be set to any value. The variable `metric_mass`, which is used to set the mass of the metric M and is used in unit conversion, is chosen in accordance with the mass of the supermassive BH Sgr A* - $M_{BH} \approx 4.26 \cdot 10^6 M_\odot$. The distance from the observer to the central object `obs_distance` is in units of M, whereas the variable `screen_dist`, which defines the distance between the observer's screen in kiloparsecs and coincides with the distance between Earth and Sgr A* (8.25 kpc). The field of view `field_view` is 200 μas. The variable `object_type = 2` designates the astrophysical object to be ray-traced as the hot spot. The variable `object_thin` states that the accretion disk around the compact object is optically thin, meaning that the accretion disk does not absorb radiation. When calculating the mask, the variable `mask_radius` is used as a scaling quantity to define the radius of the mask - for example, if `mask_radius` is equal to `0.5`, the radius of the mask is equal to `0.5*object_radius`. In each simulation, the number of rays or the number of orbital positions of the hot spot represented by the variable `number_rays` is equal to 180. This value is taken such that the image of the hot spot can be seen every 2 degrees.

In order to demonstrate the results obtained in Section 1.4, four models M1-M4 are chosen, as described in Table 2, including a comparison with a Schwarzschild BH. The radius of the

Model	R/M	R_s/M	LR	singularity	event horizon
Schwarzschild BH	0	0	✓	✓	✓
M1	2.25	2.25	✓	✓	×
M2	2.5	2.5	✓	×	×
M3	3	3	✓	×	×
M4	5	5	×	×	×

Table 2. The features of a Schwarzschild BH and simulated models M1-M4, including the star radius R/M, shell radius R_s/M and the presence of absence of LRs and singularities.

star R/M and radius of the shell R_s/M are respectively represented by variables `star_par` and `shell_par`. For all models investigated in this work, R_s is chosen to be equal to R to save simulation time. It is possible to simulate models where $R \neq R_s$, though in these cases the simulation time is significantly higher. This is due to the discontinuity of the metric component g_{rr}, for which the numerical methods require a longer computation to converge. The behaviour of such models can still be investigated in future works via a non-analytical metric, which significantly reduces the computation time.

The Schwarzschild BH and models M1-M3 are ultra compact objects (objects with a LR), of which the Schwarzschild BH and model M1 both feature singularities. However, the singularity for the Schwarzschild case is represented by the divergence in the metric components, whereas for the model M1, we use the term singularity to describe the divergence of the central pressure defined in Eq. (9). The model M4 represents a star with a smaller compacticity, which does not have a LR nor a singularity. The models are simulated for various values of `orbit_radius` and `obs_angle`. These are respectively represented by the orbital radius of the hot spot d (in units of M) and the inclination angle i (in degrees) and range from $d \in \{8M, 10M, 12M\}$ and $i \in \{20°, 50°, 80°\}$. The hot spot is imaged at 180 orbital positions for a resolution of 500 pixels. To analyze the geodesics of photons in greater detail, the mask is produced for a resolution of 2000 pixels and inclination angle $i = 0.01°$. The angle cannot be precisely zero due to the nature of the spherical coordinate system - the system becomes degenerate when $\theta = 0$, since the azimuthal angle ϕ is not well defined in this limit. Indeed, when $\theta = 0$, we have $x = r \sin\theta \cos\phi = 0$, $y = r \sin\theta \sin\phi = 0$ and $\phi = \arctan \frac{y}{x}$ becomes undefined.

3 Astrometry

Following the setup described in Section 2, we have performed the simulations for the orbits of hot spots and have produced astrometric data for the observables magnitude, centroid, and integrated flux. In this section, we summarize the results and provide a thorough analysis.

3.1 Integrated images

First, we analyze the first observable - the integrated flux of the orbits. In Fig. 5, the integrated flux of the models M1-M4 is shown for an inclination angle of $i = 80°$. For the time integrated images the inclination angles are $20°$, $50°$, see Appendix B.

The uppermost model M1 in Fig. 5 represents the Buchdahl limit. This image features a primary, secondary track and a LR (thinly dotted circle closest to the center) and thus it is qualitatively similar to a Schwarzschild BH. As the orbital radius increases, the primary and secondary tracks expand, while the LR remains unchanged.

The second model M2 shows novel features, as seen in the second row of Fig. 5. In addition to the primary and secondary tracks and the LR, the integrated images show multiple tracks in the interior. As the orbital radius of the hot spot increases, the lensed primary and secondary tracks expand similarly to BHs, and the additional trajectories in the interior become slightly smaller. The time integrated images of the model M3 $R = R_s = 3M$ in row 3 of Fig. 5 show the same components as the model $R = R_s = 2.5M$, including the primary and secondary track as well as additional tracks in the interior of the star. However, this model features only two additional tracks, whereas the previous model M2 featured three tracks, thus a qualitative difference can be observed. The model M4 in the final row of Fig. 5 resembles a compact object without a LR, consisting of the primary, secondary and the "plunge-through" track.

The following applies to all models: as the orbital radius of the hot spot increases, the gravitational deflection decreases and the image size increases proportionally to the orbital radius. It is clear that as the radius of the star increases while the mass remains constant, the compactness decreases. Comparing the models with each other, it becomes evident that the number of tracks depends on the compacticity of the star. At the Buchdahl limit $2.25M$, the star is virtually indistinguishable from a Schwarzschild BH . As the radius of the star increases, additional tracks appear in the interior and increase in size, while still remaining within the secondary track. Surpassing the radius $3M$, some of the additional trajectories in the interior disappear.

Starting from $R = 3M$, the "plunge-through" track appears. To summarize:

- $R = 2.25M$ represents a model qualitatively equivalent to a BH.
- $2.25M < R \leq 3M$ represents a model qualitatively equivalent to a horizonless ultra-compact object, e.g. solitonic boson star.
- $R > 3M$ represents a model qualitatively equivalent to a non-ultra compact object, e.g. boson star without self interactions.

By increasing the resolution of the image to 2000 pixels and tracing the geodesics associated to illuminated pixels on the circles in the yz-plane for an inclination angle $i = 0.01°$, the trajectories of photons can be analyzed with higher precision. Counting the times the incoming photon crosses the equatorial plane $xy = const$ after emission determines the type of the corresponding track - a primary track corresponds to photons that do not cross the equatorial plane after emission; a secondary track to photons that cross the plane once; and LRs to photons

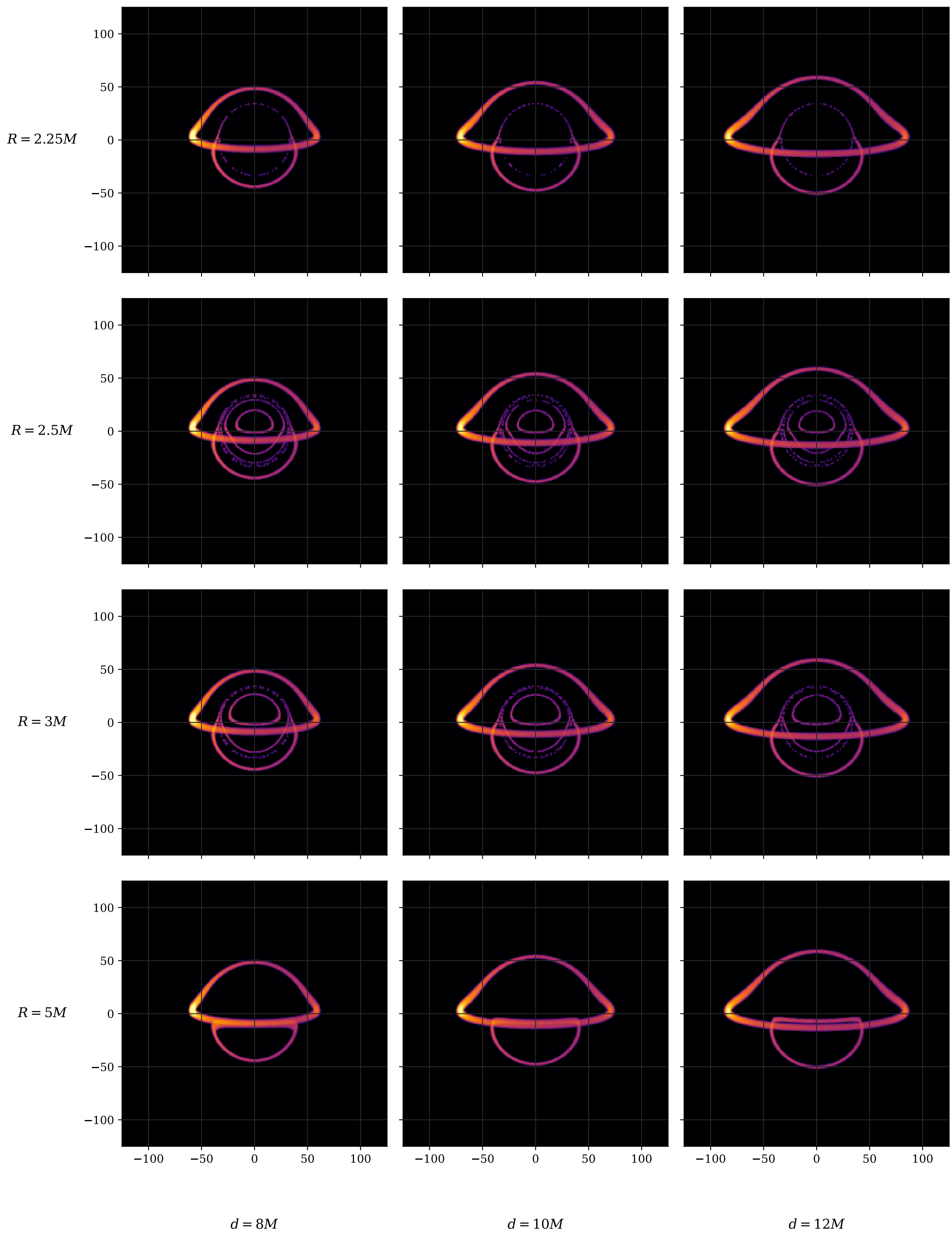

Figure 5. Time integrated images of models M1-M4 ($R = R_s \in \{2.25M, 2.5M, 3M, 5M\}$) for orbital radii $d \in \{8M, 10M, 12M\}$ at an inclination angle of $80°$. Models M1 and M4 resemble a Schwarzschild BH and a boson star respectively, analogous to [28], while models M2, M3 feature novel trajectories in the interior.

that cross the plane more than once (orbiting the object at least once before being reaching the observer). When the photon is slightly deflected (less than $90°$) off its original course in the

yz-plane, it is a part of the primary track. A photon deflected more than 90° and thus making a half turn around the object corresponds to a secondary image. Whenever a "loop" appears, the emitted photon follows a trajectory close to the LR for a certain period of time before being deflected to the observer's screen. Note that additional loops are also indicative of a LR, since in theory LRs correspond to photons that orbit the object an infinite amount of times before being deflected. In order to obtain several loops around a LR using this software, the value of the impact parameter needs to be fine-tuned close to the critical impact parameter $b_c = 3\sqrt{3M}$. Yet, since the image has a finite resolution with a relatively small amount of pixels, the likelihood of finding a pixel with an impact parameter very close to the critical impact parameter is small and thus we do not observe additional loops. The value of the inclination angle is chosen to be close to zero to ensure that the crossing of the xy-plane can be seen from a single yz-graph and no information is lost to other directions.

The integrated flux of the models M1-M4 for an orbital distance $d = 8M$ and inclination angle $i = 0.01°$ for a 2000 pixel resolution is shown in Fig. 6 with traced geodesics marked in red.

Consider the model M1 first. The tracks corresponding to traced pixels are numbered from 1-3, starting from the most outward track and moving towards the center. The types of tracks are deduced from geodesics in the yz-plane, as described in the previous paragraph. The geodesics of pixels on each of the tracks can be seen in Fig. 7, showing a top-down view of the trajectories of the photons. The solid black line represents the orbit of the hot spot in the xy-plane and the dashed black line represents the unstable LR $r_{LR} = 3M$. The observer is situated at $y = 0$, $z = 1000M$. Note that the trajectories corresponding to the primary and secondary track intersect with the hot spot orbit at $y = -8M$, $y = 8M$, but the trajectory representing a LR track does not - this is due to the fact that these geodesics are very sensitive to initial conditions. Therefore, tracing the geodesic of an illuminated photon might provide as with a trajectory that does not connect the hot spot to the observer, as is the case in our result. However, the origin of the geodesic remains the same - while we might not know the exact trajectory of the photon, we know that this corresponds to a LR contribution.

As this model represents the Buchdahl limit, all photons with an impact parameter larger than the critical impact parameter b_c are deflected and form either the outer primary (track 1) or secondary track (track 2) further towards the center. The innermost track 3 represents a photon with an impact parameter close to b_c, which reaches the observer's screen after orbiting the Schwarzschild LR at $r_{LR} = 3M$. Any photon with a smaller impact parameter becomes trapped within the potential well depicted in Fig. 2. This behaviour is similar to a Schwarzschild BH, though not identical, since in the latter case, photons become trapped due to the event horizon.

The geodesics of model M2 are shown in Fig. 8. Note that this particular model satisfies the condition $2.25M < R < 3M$; therefore, the model must feature an additional stable LR at a radius dependent on R, in addition to the Schwarzschild BH LR $r_{LR} = 3M$. In the case $R = 2.5M$, the critical value in Eq. (13) is found to be $\bar{r}_{LR} \approx 1.86M$. The solid black line in Fig. 8 represents the orbit of the hot spot in the xy-plane, the dashed black line the unstable LR $r_{LR} = 3M$ and the dash-dotted line the stable LR $\bar{r}_{LR} \approx 1.86M$.

As can be seen from Fig. 8, the first and widest track corresponds to the primary track - the photon is deflected slightly off-course, without crossing the equatorial plane. The photons of tracks 2 and 7 behave similarly, making a half turn around the star - these are examples of photons forming a secondary track. The outermost secondary track is deflected in a continuous manner - the curvature of the trajectory changes at a constant rate. However, the innermost secondary track appears to be bent - the curvature changes abruptly after crossing $r_{LR} = 3M$ and before crossing the radius $\bar{r}_{LR} \approx 1.86M$. This is due to the stable LR, which creates a potential well (see model $R = 2.5M$ Fig. 2) - after crossing the edge, the photon is pulled towards the

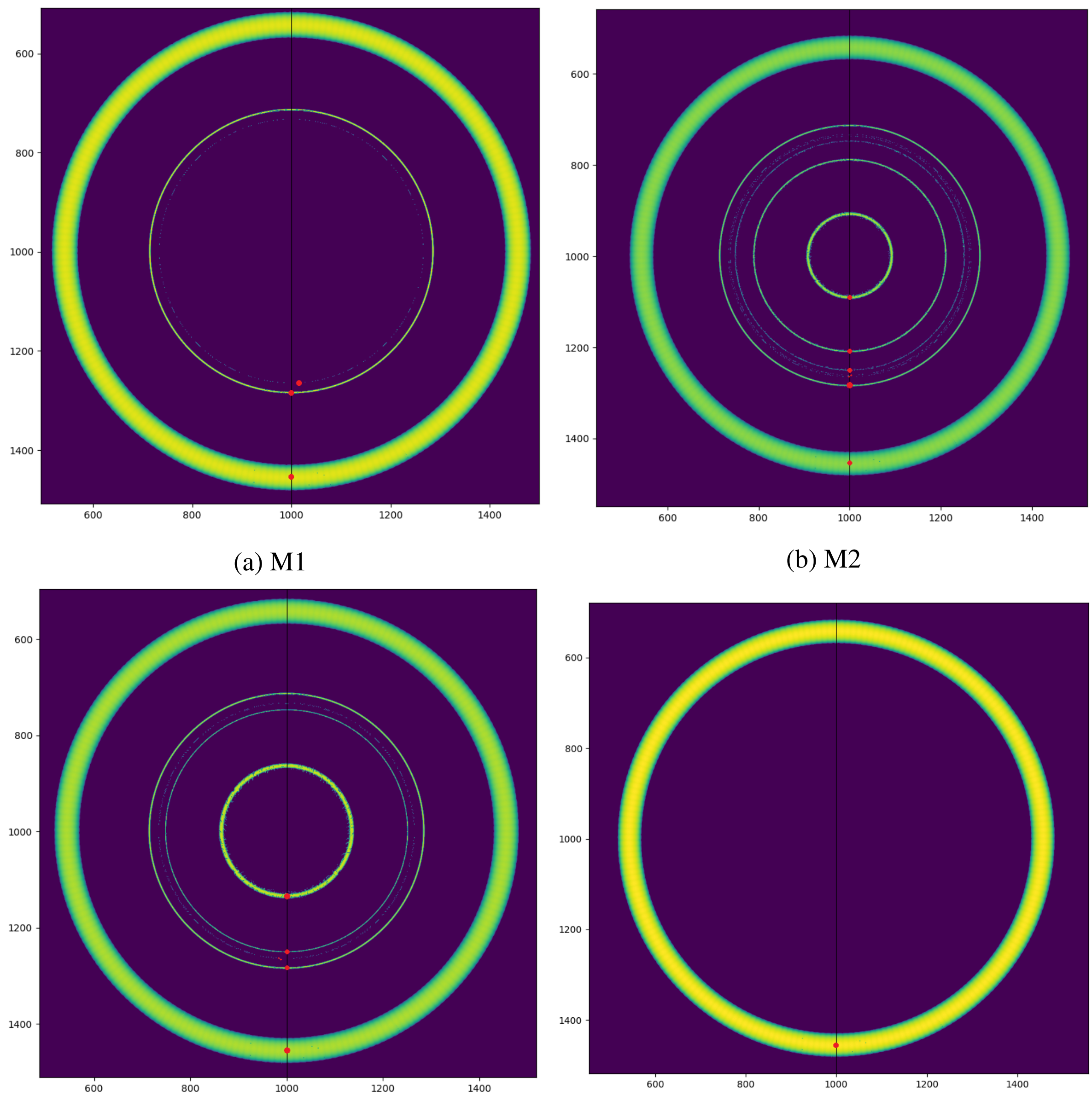

(a) M1

(b) M2

(c) M3

(d) M4

Figure 6. The integrated flux of the models M1-M4, at an orbital radius $d = 8M$ and inclination angle $i = 0.01°$. The red dots on the line $y = 1000M$ represent pixels with traced geodesics, numbered from 1 to a maximum of 7, starting from the outside and moving towards the center.

bottom of the well.

Tracks 3-6 correspond to LR contributions, which feature interesting properties. Track 3 in the center image in Fig. 8 represents a photon that orbits the unstable LR, makes an additional loop inside the stable LR and is then deflected. Since the track closely follows the unstable LR, the impact parameter of this photon is close to the critical impact parameter $b_c = 3\sqrt{3}M$. The photon on track 4 follows a similar trajectory, although being less affected by the outer LR. Notice the similar impact parameters but different escape trajectories of tracks 3 and 4. This implies that these photons are associated with the same LRs are emitted from the hot spot while it is located in different orbital positions. These impact parameters must be smaller than b_c, but still close to that value, because otherwise they would not be able to cross the unstable LR. Track 5 shows a different trajectory - the photon does not follow the exterior LR, but crosses it

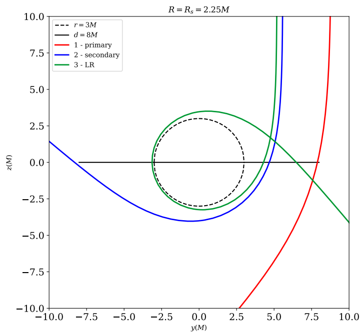

Figure 7. Geodesics of the model M1 in the yz-plane, at an orbital radius $d = 8$ and inclination angle $i = 0.01°$. The red curve represents a photon on the primary track, the blue line corresponds to the secondary track and the green line represents photons travelling on LRs. The solid black line corresponds to the orbital radius, the dashed line is the unstable LR $r_{LR} = 3M$.

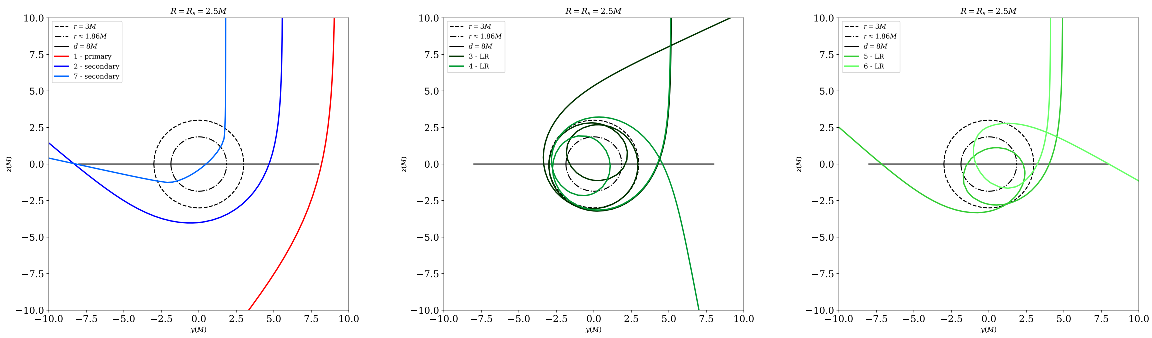

Figure 8. Geodesics of the model M2 in the yz-plane, at an orbital radius $d = 8$ and inclination angle $i = 0.01°$. The red curve (left image) represents a photon on the primary track, blue lines (left image) correspond to secondary tracks and green lines (center and right images) represent photons travelling on LRs. The solid black line corresponds to the hot spot orbital radius, the dashed line is the unstable LR $r_{LR} = 3M$ and the dash-dotted line is the stable LR $\bar{r}_{LR} \approx 1.86M$.

entirely and makes a loop caused by the interior LR. Since the impact parameter is relatively small compared to b_c, the unstable LR has little influence on this trajectory. Yet, the existence of a loop implies a contribution from a LR - thus the trajectory is caused mainly by the stable LR.

As the impact parameter further decreases on track 6, the photon performs a loop which does not align with either of the LRs. Since the impact parameter is much smaller than b_c, the deflection caused by the unstable LR becomes non-existent, while the effect from the interior LR increases.

To conclude, the tracks represent the following: 1) primary track, 2) secondary track, 3-6) LRs, 7) secondary track. Comparing this to the BH equivalent model M1, while the primary, secondary track and the LR seen in the BH model are present, an additional image of the secondary track appears closest to the center and additional trajectories representing LRs appear between the innermost image of the secondary track and the original BH LR. Another noteworthy aspect regarding the model M2 is the behaviour of photons inside the LRs - photons are diverted inside the unstable LR $r_{LR} = 3M$ and perform loops inside this radius. The exterior unstable and interior stable LRs have a combined influence on the photons in both cases, but one LR dominates over the other dependent on the impact parameter. Tracks 3-4 represent photons with impact parameters close to the critical value b_c, with contributions dominated by the unstable LR. Tracks 5-6 represent photons with impact parameters much smaller than b_c, in which case the trajectory is caused mainly by the stable LR.

Let us now compare our results with the ones for the model M3, whose image of the integrated flux features fewer trajectories in the interior. As $R = 3M$, a degenerate pair of LRs is predicted to appear at $r_{LR} = 3M$. Similarly to before, the trajectories of photons for the model M3 are shown in Fig. 9.

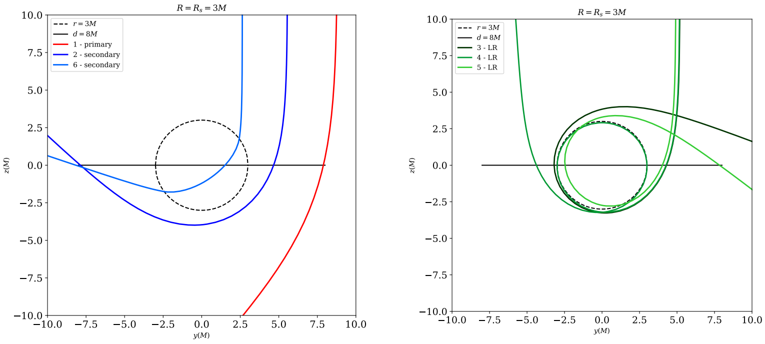

Figure 9. Geodesics of the model M3 in the yz-plane, at an orbital radius $d = 8$ and inclination angle $i = 0.01°$. The red curve (left) represents a photon on the primary track, blue lines (left) correspond to secondary tracks and green lines (right) represent photons travelling on LRs. The solid black line corresponds to the orbital radius $d = 8M$, the dashed line is the degenerate LR pair $r_{LR} = 3M$.

Again, the type of tracks in the integrated image can be inferred from the geodesic behaviour. The first track corresponds to the primary track, mirroring the previous models' first track. Tracks 2 and 6 representing the secondary tracks are visually identical to tracks 2 and 7 in model M2. The interior secondary track bends as the photon crosses the border $r_{LR} = \bar{r}_{LR} = 3M$, caused by the degenerate LR pair at this radius. The remaining tracks 3-5 depict LRs, however, as there is no interior LR, the photons perform a single loop at most. Tracks 3-4 follow the trajectory of the degenerate LR $r = 3M$, with track 4 performing a loop aligning with the LR, corresponding to an impact parameter very close to b_c and track 3 being less deflected, corresponding to a smaller impact parameter. Track 5 is similar to track 3, but due to having a smaller impact parameter, the photon crosses the LR radius $3M$ while performing a loop. These tracks represent the same LR but are associated with different orbital positions of the hot spot.

In conclusion, the tracks of the model M3 represent the following: 1) primary track, 2) secondary track, 3-5) LRs, 6) secondary track. Comparing this model with the previous model M2, the similarities become evident - the primary, secondary tracks and the LR of the Schwarzschild BH remain unchanged, a novel image of the secondary track appears in the center and three additional LRs appear between the BH light ring and the innermost secondary track. Differing from the model M2, the number of novel tracks corresponding to LRs in this model (3) in the interior is smaller than in the previous (4). This is due to the degeneracy of the LR at $R = 3M$. In addition, the photons make no loops inside the radius $r_{LR} = 3M$, as is obvious from the absence of the interior LR. The fifth track resembles track 6 of the previous model M2 - thus the innermost LRs of the models are caused by similar trajectories - by photons with small impact parameters.

For comparison, consider the geodesics of the final model M4 in Fig. 10.

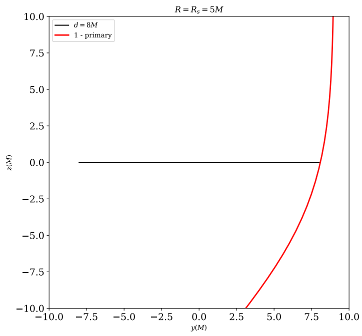

Figure 10. Geodesics of the model M4 in the yz-plane, at an orbital radius $d = 8$ and inclination angle $i = 0.01°$. The single red curve represents a photon on the primary track. The solid black line corresponds to the orbital radius $d = 8M$.

This model $R = 5M > 3M$ represents the least compact star of the analyzed models. In this case, incoming photons are allowed to pass through the object similarly to models M2-M3. However, due to the small compacticity of the star, they are deflected to form only the primary track, as is evident from the corresponding image in Fig.
reffig:5 in Appendix B.

To analyze the motion of photons in greater detail, consider the full geodesic congruence of the models M1-M4 in Fig. 11, depicting the traced trajectories of pixels on the line $y = 1000M$, separated by 20 pixel intervals.

In model M1, photons with impact parameters much smaller than b_c are deflected to perform either the primary or secondary track. Photons with an impact parameter close to $3\sqrt{3}M$ perform loops, while photons with an impact parameter above b_c are absorbed by the compact object. In the following models M2-M4, the absence of this horizon allows for additional trajectories in the interior, forming either secondary tracks or LRs. In model M2, loops are performed according to two LRs - the exterior unstable LR and interior stable LR, whereas in model M3, the loops are caused only by the degenerate LR pair. The model M4 represents a case where no LRs appear due to the small compacticity of the star.

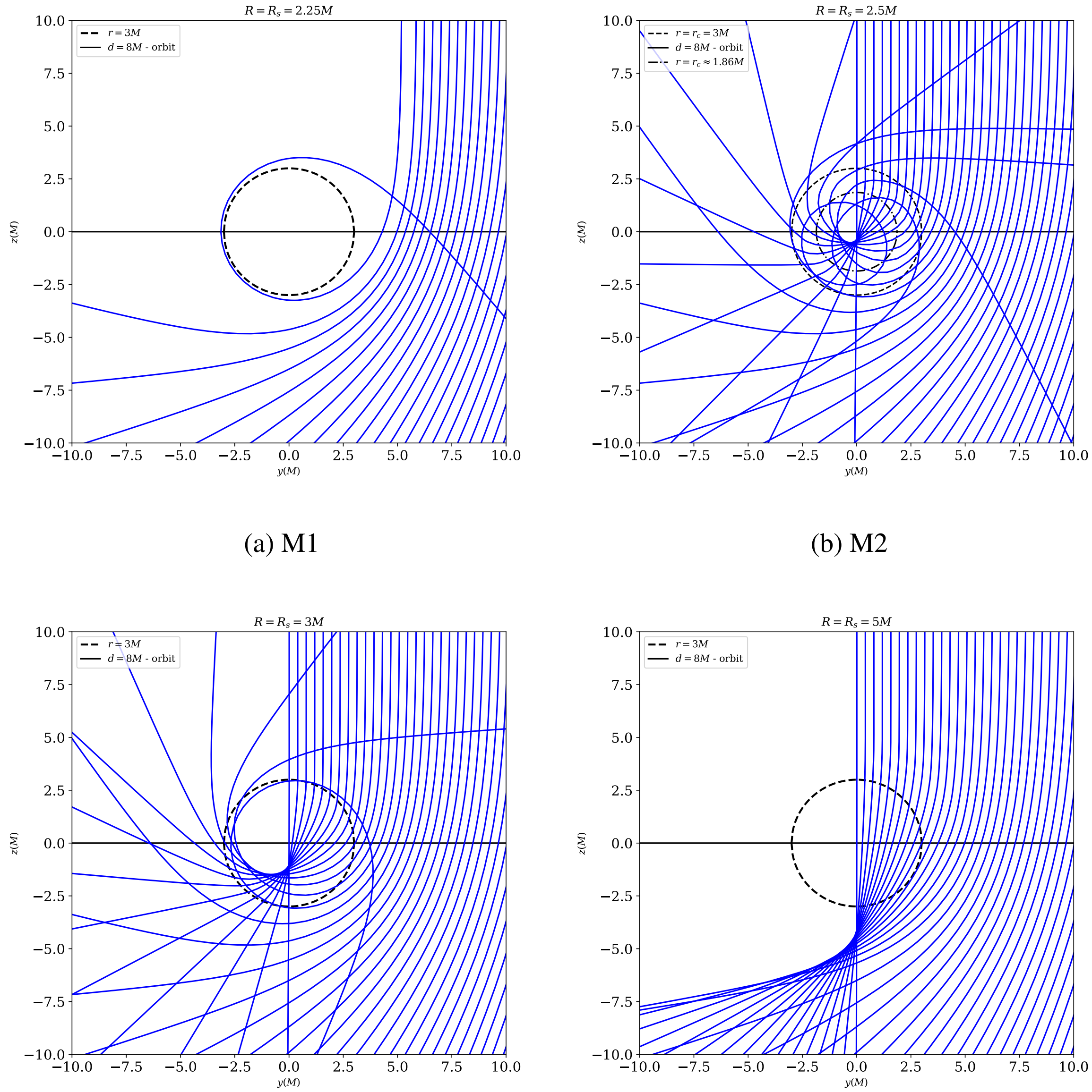

(a) M1

(b) M2

(c) M3

(d) M4

Figure 11. The geodesics of photons for the models M1-M4, at an orbital radius $d = 8M$ and inclination angle $i = 0.01°$. The pixels are traced on the line $y = 1000M$, separated by 20 pixel intervals. See text for details.

3.2 Temporal sequence and magnitudes

To better visualize the motion of the hot spot during the orbital period, consider the temporal sequence shown in Fig. 12, showing the lensed image of the hot spot at a particular point in the orbit. The times are chosen such that the primary image of the hot spot is at same positions and to reflect noteworthy features, such as the appearance of a LR.

The temporal sequence shows that independently of the model, the primary track is visible at all times during the period, increasing in magnitude as it approaches from the left and decreasing as it recedes on the right. As seen from the top row representing the model M1, the secondary track is present during the first half of the orbit and at the end of the orbit, the LR appears. For models M2 and M3 in the second and third row respectively, an additional image of the secondary

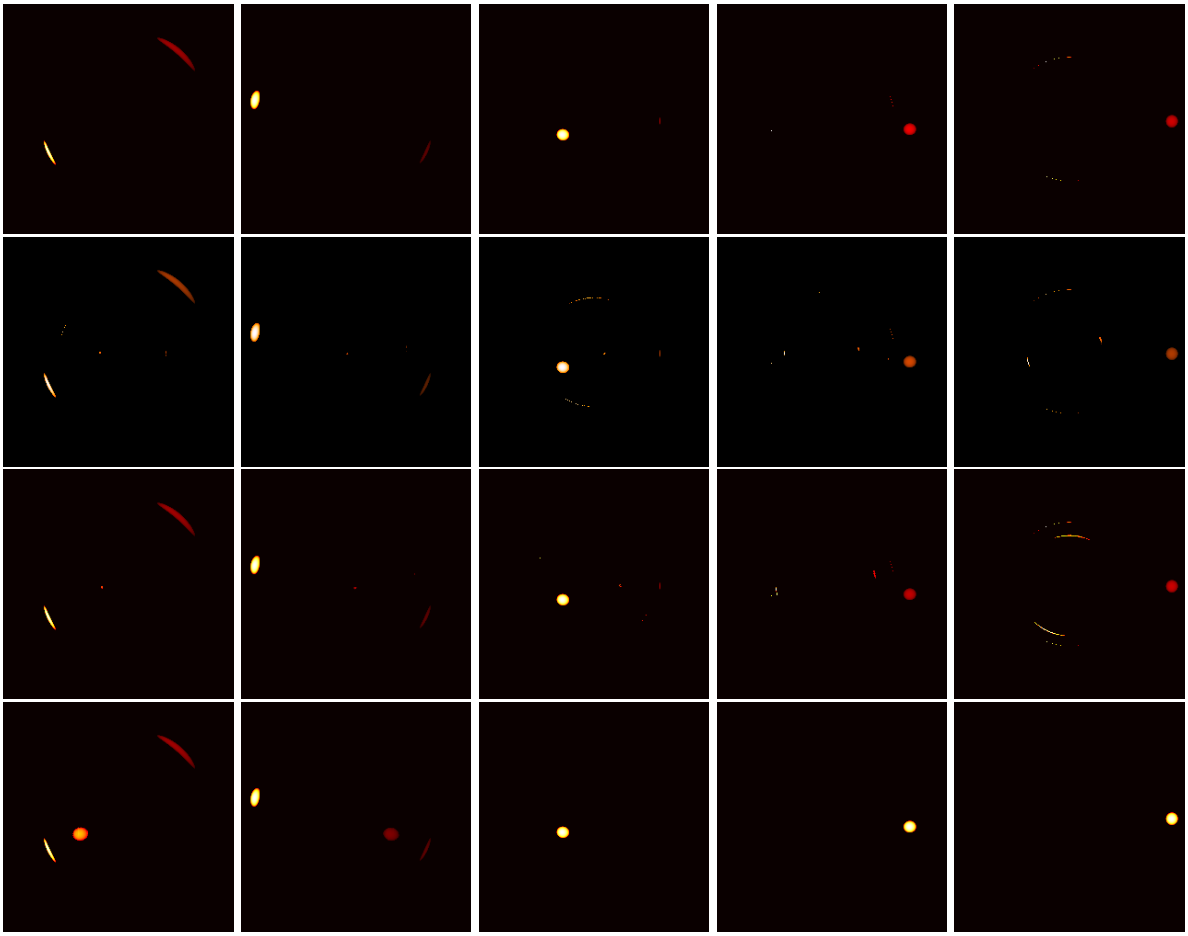

(a) $t \approx 0.11T$ (b) $t \approx 0.22T$ (c) $t \approx 0.44T$ (d) $t \approx 0.66T$ (e) $t \approx 0.77T$

Figure 12. Temporal sequence showing the flux at different points of the orbital period for models M1-M4 for $i = 80°$, $d = 8M$.

track appears closest to the center and is present for the entirety of the period. Additional LRs appear at $t \approx 0T$, $t \approx 0.4T$ and $t \approx 0.6T$, the latter of which represents the Schwarzschild LR. Due to the high inclination angle, the secondary image is split into two at the end of the orbit, creating the top part of the innermost track and the bottom part of the second innermost track. The image of the model M3 behaves similarly, with an exception regarding the end of the orbit - the final LR and secondary image appear simultaneously, while in model M2, they appear with a slight delay. The model M4 features the secondary and plunge-through track, which appear separately, meld into one and separate again before the end of the first half of the period.

The temporal magnitudes m_k for a full orbit defined in Eq. (17) are shown in Fig. 13 for various orbital radii ($d \in \{8M, 10M, 12M\}$) and inclination angles ($i \in \{20°, 50°, 50°\}$).

Consider the model M1 first, shown in the topmost row of Fig. 13 in red. The magnitude is a symmetrical curve with one peak in cases where the inclination angle is $i = 20°$ and $i = 50°$. For the angle $80°$, two additional peaks can be seen - one peak, which is higher in magnitude and appears slightly before the main central peak, and one lower peak near the end of the orbital period. The main central peak forms due to the relativistic Doppler effect - the hot spot is blueshifted and brighter as it approaches; redshifted and less brighter as it recedes. The extra peaks appearing at $80°$ are caused by the appearance of the secondary image, which is absent for smaller angles (see Fig. 15 in Appendix B). Decreasing the orbital distance produces higher peaks - this is due to increased velocity of the hot spot, which produces stronger relativistic

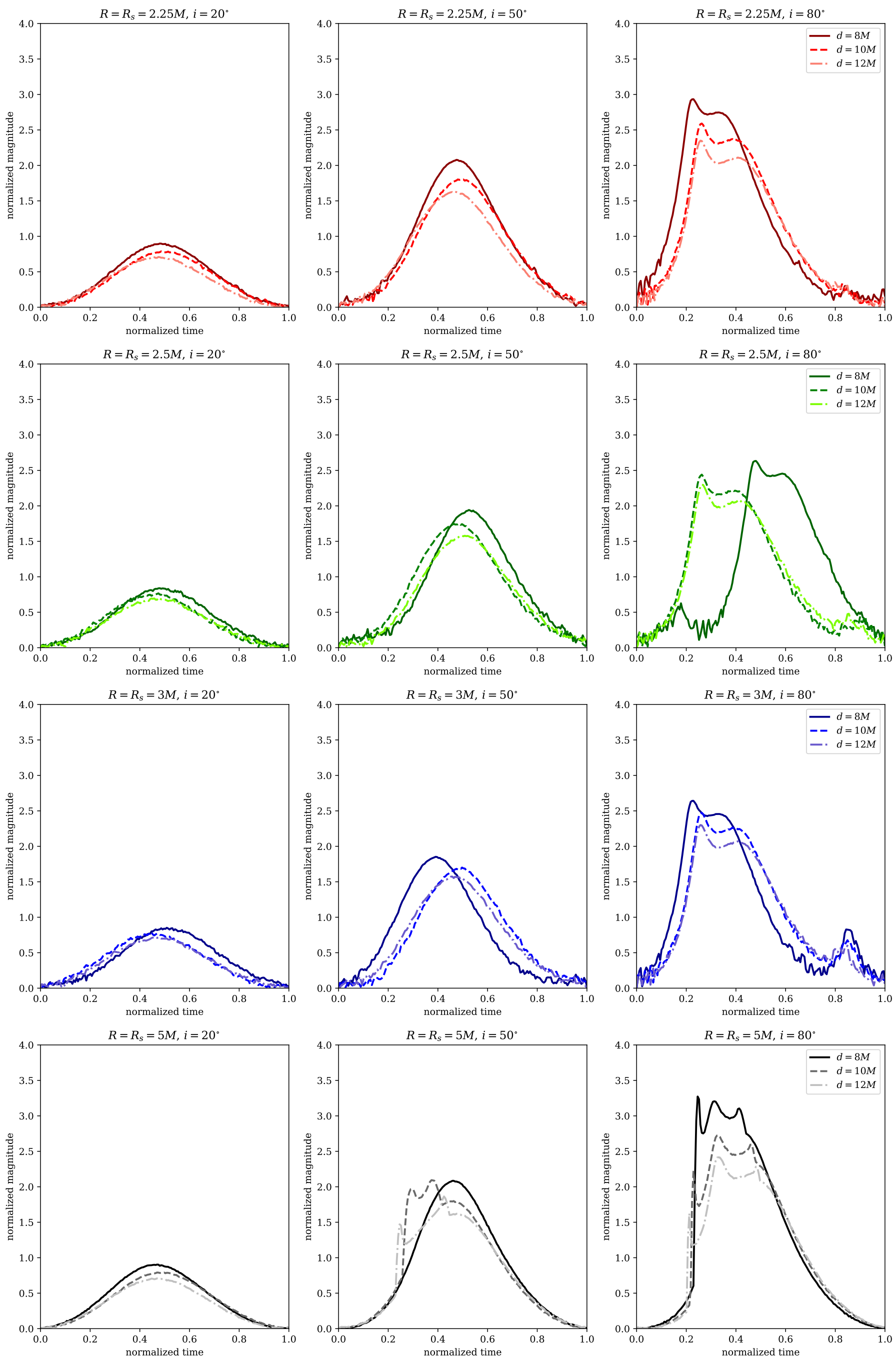

Figure 13. Temporal magnitudes of the hot spot for models M1-M4 for inclination angles $i \in \{20°, 50°, 80°\}$ and for orbital radii $d \in \{8M, 10M, 12M\}$. See text for analysis.

Doppler- and beaming effects [42]. This is also the cause of increased intensity as the inclination angle increases.

As shown in the temporal sequence, the primary track is present throughout the entire orbital period, while the pixels corresponding to the LR appear sporadically through-out the period. Note that the temporal sequence is analyzed for $i = 80°$ and thus is only relevant for the rightmost plots in Fig. 13. As the intensity of the flux is far greater in the primary and secondary tracks than the LRs, the main contributors to the magnitude are photons on the primary and secondary track. One can also observe slight deviations from the continuous curve or so-called "noise". This is caused by the presence of LRs - as only a small fraction of photons become trapped in the LR, the tracks are not continuous due to the low resolution of the image, which is reflected in the data at random intervals. In the low flux region, additional noise can be seen - since the magnitude is a logarithmic quantity, the contribution from the LR becomes larger at smaller values.

The models M2 and M3 depicted in Fig. 13 in green and blue respectively feature two types of contributions, one corresponding to additional LR tracks which form in the interior and the other to the new secondary image closest to the center of the star. The tracks appear one after the other in the temporal sequence, the outermost tracks being shown at the beginning of the orbital period and the tracks closer to the center being shown as time progresses. But, since the intensity of the flux of photons on LR tracks is comparatively small, these contributions are represented by very small deviations from the main curve of the magnitude, which cannot be distinguished from numerical noise. For the model M2, the additional secondary track in the center appears at all times and at 80 degrees splits into two - this increases the magnitude of the smaller peak at the end of the period and in turn lessens the magnitude at other points of the period, compared to model M1. For the model M3 at 80 degrees, this increase in the second peak is greater due to the smaller amount of LR tracks.

As for the final model M4 (shown in the bottom row of Fig. 13), the graphs show a double-hump arising at $d = 10$, $i = 50°$. Supported by the visual integrated flux in Fig. reffig:5, these extra peaks are caused by the appearance of the secondary image with the "plunge-through" track. The tracks appear as one (first hump), separate (dip in the magnitude) and are then merge again (second hump) as time progresses and disappear (are red-shifted) before the primary image reaches its leftmost position - in other words, before the first half of the orbital period ends. As the orbital distance of the hot spot increases, the joined track appears for a longer period. In the case $80°$, the contribution of the distinct secondary image can be seen, forming an extra peak in-between the two peaks caused by the "plunge-through" track. Note that for this model, the magnitude is free of noise originating from pixels on the LR, since no LRs are present.

3.3 Centroids

The centroids as defined in Eq. (18) can be seen for a whole orbit in Fig. 14. The plots show the movement of the centroid - weighted average of the intensity as a singular point - during the orbital period. Note that the x- and y-axis of these plots are inverted in regard to the integrated images. Increasing the orbital radius increases the size of the centroid orbit, since the hot spot orbits at greater distances. Consider the model M1 first. For an observation angle of $20°$, the centroid track is approximately circle with some noise originating from the LR when it is present. As the inclination angle increases, the primary track becomes asymmetric and the centroid trajectory is distorted. As the inclination angle increases to $80°$, the centroid orbit is further deformed and a cusp appears. This is caused by the appearance of the secondary track causing the centroid to be pushed further towards the center. With the increase of the inclination angle, the trajectory of the centroid is flattened along the y-axis, as the image deviates from the circle and approaches a distorted ellipse. The lower part of the primary track approaches the center of the image (see Fig. 15 in Appendix B). As the primary image dominates on the left side of the centroid trajectory, the left side resembles a distorted ellipse, whereas on the right side, the appearance of the LR and the secondary track pushes the centroid inward.

Focusing on the models M2-M3, additional peaks can be seen on the right side of the centroid track. These are caused by the extra image of the secondary track, interior stable LR and the increasing dominance of LRs - as they are situated closer to the center, the centroid moves closer to the center with their appearance. Since LRs appear at different orbital positions, they are

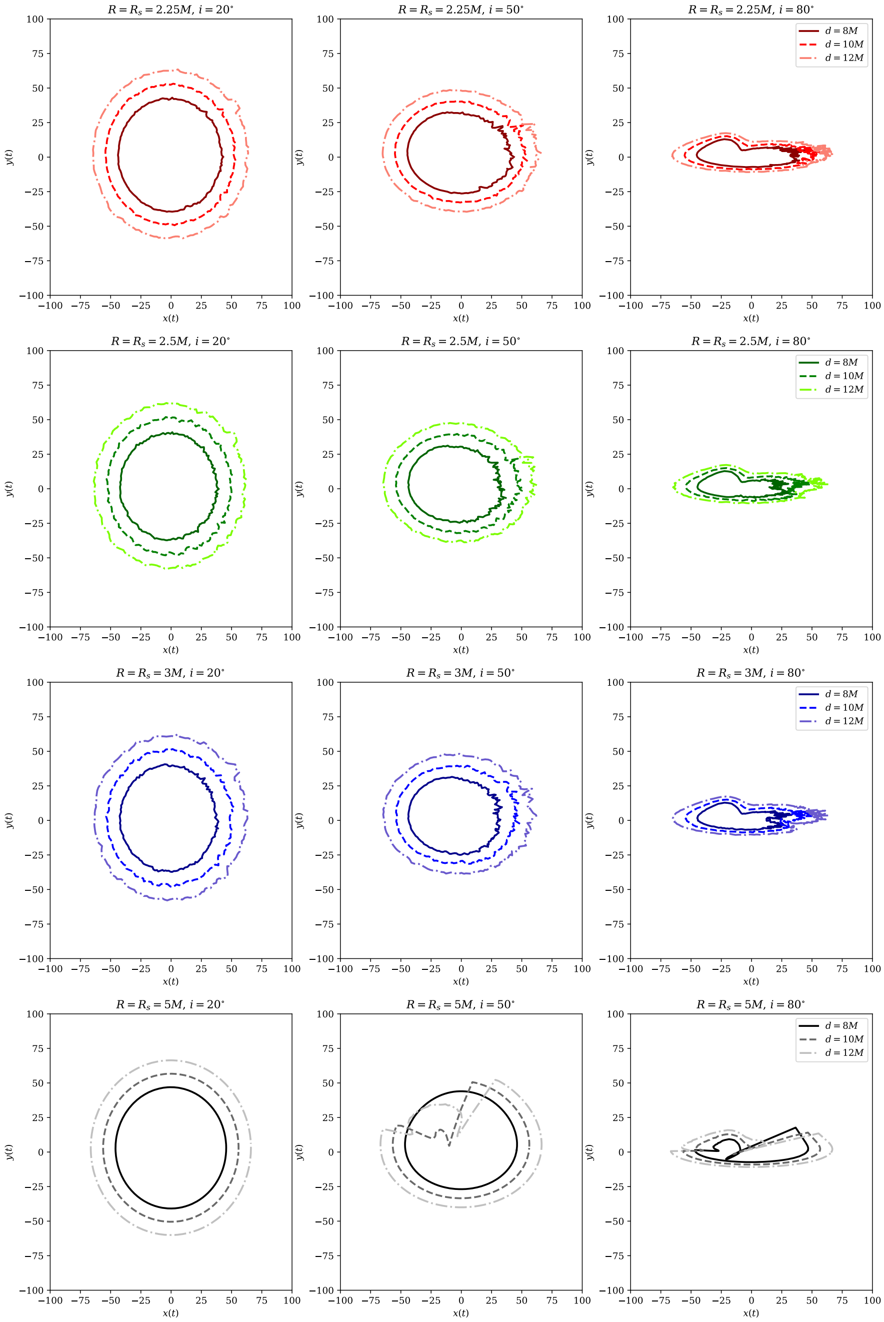

Figure 14. Centroid trajectories during the orbital period for models M1-M4 for angles $i \in \{20^\circ, 50^\circ, 80^\circ\}$ and orbital radii $d \in \{8M, 10M, 12M\}$. See text for analysis.

represented in the track as distinct peaks. Small differences can be observed between the centroid tracks of models M2 and M3 due to different contributions of LRs.

Regarding the model M4, the noise from the LRs is absent and starting from the orbital distance $d = 10M$ at $i = 50°$, additional peaks appear before the main central peak due to the secondary track and the plunge-through track. This can be explained by Fig. 18, showing that at lower inclination angles than $50°$ and smaller orbital radii than $d = 10M$ only the primary image can be seen. As additional tracks appear close to the center of the image, the centroid orbit is deformed towards the center. Differing from the previous models, the centroid tracks show a sudden hump on the left side of the image, corresponding to the appearance of the secondary track, which creates a smaller bump near the center of the image due when it combines with the plunge-through track. Note that this bump is not symmetrical with respect to the drops corresponding to the appearance and disappearance of the additional track due to the Doppler shift - the intensity decreasing on the right side of the integrated image. As the orbital distance d increases, a bigger hump forms due to the increased width of the additional track.

In summary, the centroid's behaviour depends on the number of tracks present for a given model. As the inclination angle increases, the centroid trajectory changes from a circle to a distorted ellipse, with additional smaller details. For models M1-M3, the presence of one or more LRs produces noise and additional peaks in the centroid track. For all models, a shift towards to the center appears on the centroid track due to the appearance of a secondary track, which for the model M4 combines with the plunge-through track. For the final model, the shape of the centroid track differs due to the absence of a LR.

Conclusions

In this work, the visual signatures of hot spots orbiting compact fluid spheres were analyzed. Followed by analysis on the effective potential and the existence and stability of LRs, the models were simulated using the software GYOTO and observables such as the integrated flux, magnitudes and centroids were produced. Thus the effect of LRs and horizons on the visual properties of a hot spot was studied.

The model analyzed in this work, consisting of a piecewise metric of an interior and exterior Schwarzschild solution separated by a thin shell, produces different results dependent on the radius of the star R and the radius of the shell R_s. At the Buchdahl limit $R = R_s = 2.25M$, the visual signature of the hot spot is qualitatively indistinguishable from a Schwarzschild BH. As the compacticity of the fluid star decreases in the range $2.25M < R = R_s < 3M$, results indicate the existence of an additional interior stable LR with a radius $\bar{r}_{LR}$ dependent on the radius of the star R, which produces additional visual signatures. In the integrated flux of the model, additional LR tracks and a new secondary track can be observed in the center of the image. These tracks form due to new types of trajectories caused by the presence of a stable interior LR. In the temporal magnitudes, the main noticeable difference is the increased height of the second peak near the end of the orbital period, which corresponds to the secondary track.

As the star radius R increases further in the range $2.25M < R < 3M$, the radius of the interior LR increases until it coincides with the Schwarzschild LR at $R = 3M$, thus producing a degenerate LR pair. Compared to the Schwarzschild case, the integrated flux features additional tracks similarly to the previous case, but due to the degeneracy of the LR, the number of additional LR tracks is smaller. Once the star radius surpasses the value $3M$, no LR appear. Due to the absence of an event horizon, the integrated flux of the model consists of the primary track, secondary track and the plunge-through track, which qualitatively resembles a horizonless non-ultra compact object.

This work intends to produce a wider perspective into the study of BHs and other ECOs by analyzing the motion of hot spots around compact objects. By comparing the results of ECO models with the classic BH model, the evidence for BHs can be investigated with more precision and better-defined limits. We have found that certain configurations of the fluid star model investigated in this work are visually indistinguishable from BHs and therefore serve as valid BH mimickers. However, we have also found configurations where the observables of the hot spot feature slight differences, which could be used to potentially distinguish fluid stars from other compact objects. Due to upcoming advances in very-long-baseline interferometry – for example, the next generation of the Event Horizon Telescope –, this distinction could potentially be observed.

The implementation of a new metric in GYOTO allows to simulate more complicated models in future works - configurations of the thin shell model where $R \neq R_s$, using a non-analytical metric, and additional models consisting of a piecewise metric, e.g. a gravastar. Furthermore, since the GYOTO software is not equipped to efficiently calculate the motion of photons around objects with a stable LR, additional features could be introduced to the software. As the precision of experiments in testing phenomena close to the event horizon rises, so does the hope of distinguishing BHs from other compact objects.

References

[1] B. P. Abbott et al. (The LIGO Scientific and Virgo Collaborations). “Observation of Gravitational Waves from a Binary Black Hole Merger”. *Phys. Rev. Lett.* 116 (6 Feb. 2016), p. 061102. DOI: 10.1103/PhysRevLett.116.061102.

[2] B. P. Abbott et al. (The LIGO Scientific and Virgo Collaborations). “GWTC-1: A Gravitational-Wave Transient Catalog of Compact Binary Mergers Observed by LIGO and Virgo during the First and Second Observing Runs”. *Physical Review X* 9.3 (Sept. 2019). DOI: 10.1103/physrevx.9.031040.

[3] B. P. Abbott et al. (The LIGO Scientific and Virgo Collaborations). “GWTC-2: Compact Binary Coalescences Observed by LIGO and Virgo during the First Half of the Third Observing Run”. *Physical Review X* 11.2 (June 2021). DOI: 10.1103/physrevx.11.021053.

[4] B. P. Abbott et al. (The LIGO Scientific and Virgo and KAGRA Collaborations). “GWTC-3: Compact Binary Coalescences Observed by LIGO and Virgo During the Second Part of the Third Observing Run” (Nov. 2021). DOI: 10.48550/ARXIV.2111.03606.

[5] K. Akiyama et al. (The Event Horizon Telescope Collaboration). “First M87 Event Horizon Telescope Results. I. The Shadow of the Supermassive Black Hole”. *The Astrophysical Journal Letters* 875.1 (Apr. 2019), p. L1. DOI: 10.3847/2041-8213/ab0ec7.

[6] K. Akiyama et al. (The Event Horizon Telescope Collaboration). “First M87 Event Horizon Telescope Results. IV. Imaging the Central Supermassive Black Hole”. *Astrophysical Journal Letters* 875 (Apr. 2019).

[7] K. Akiyama et al. (The Event Horizon Telescope Collaboration). “First M87 Event Horizon Telescope Results. V. Physical Origin of the Asymmetric Ring”. *Astrophys. J. Lett.* 875.1 (2019), p. L5. DOI: 10.3847/2041-8213/ab0f43. arXiv: 1906.11242 [astro-ph.GA].

[8] K. Akiyama et al. (The Event Horizon Telescope Collaboration). “First Sagittarius A* Event Horizon Telescope Results. I. The Shadow of the Supermassive Black Hole in the Center of the Milky Way”. 930 (May 2022).

[9] R. Penrose. “Gravitational collapse: The role of general relativity”. *Riv. Nuovo Cim.* 1 (1969), pp. 252–276. DOI: 10.1023/A:1016578408204.

[10] M. Dafermos. “Black Holes Without Spacelike Singularities”. *Communications in Mathematical Physics* 332.2 (May 2014), pp. 729–757. DOI: 10.1007/s00220-014-2063-4.

[11] B. Carter. “Axisymmetric Black Hole Has Only Two Degrees of Freedom”. *Phys. Rev. Lett.* 26 (6 Feb. 1971), pp. 331–333. DOI: 10.1103/PhysRevLett.26.331. URL: https://link.aps.org/doi/10.1103/PhysRevLett.26.331.

[12] S. W. Hawking. “Information loss in black holes”. *Physical Review D* 72.8 (Oct. 2005). DOI: 10.1103/physrevd.72.084013. URL: https://doi.org/10.1103%2Fphysrevd.72.084013.

[13] L. M. Krauss. “Dark Matter and Inflation”. *Gen. Rel. Grav.* 17 (1985), p. 89. DOI: 10.1007/BF00760108.

[14] D. J. Marsh. “Axion cosmology”. *Physics Reports* 643 (July 2016), pp. 1–79. DOI: 10.1016/j.physrep.2016.06.005.

[15] T. Clifton et al. “Modified gravity and cosmology”. *Physics Reports* 513.1-3 (Mar. 2012), pp. 1–189. DOI: 10.1016/j.physrep.2012.01.001. URL: https://doi.org/10.1016%2Fj.physrep.2012.01.001.

[16] D. J. Kaup. "Klein-Gordon Geon". *Phys. Rev.* 172 (5 Aug. 1968), pp. 1331–1342. DOI: 10.1103/PhysRev.172.1331. URL: https://link.aps.org/doi/10.1103/PhysRev.172.1331.

[17] B. R. Iyer, C. V. Vishveshwara, and S. V. Dhurandhar. "Ultracompact (R < 3 M) objects in general relativity". *Classical and Quantum Gravity* 2.2 (Mar. 1985), p. 219. DOI: 10.1088/0264-9381/2/2/013.

[18] P. O. Mazur and E. Mottola. "Gravitational vacuum condensate stars". *Proceedings of the National Academy of Sciences* 101.26 (June 2004), pp. 9545–9550. DOI: 10.1073/pnas.0402717101.

[19] V. Cardoso and P. Pani. "Testing the nature of dark compact objects: a status report". *Living Reviews in Relativity* 22.1 (July 2019). DOI: 10.1007/s41114-019-0020-4.

[20] N. K. Johnson-McDaniel et al. "Constraining black hole mimickers with gravitational wave observations". *Physical Review D* 102.12 (Dec. 2020). DOI: 10.1103/physrevd.102.123010.

[21] K. Schwarzschild. "Über das Gravitationsfeld einer Kugel aus inkompressibler Flüssigkeit nach der Einsteinschen Theorie". In: *Sitzungsberichte der Königlich Preussischen Akademie der Wissenschaften zu Berlin*. Mar. 1916, pp. 424–434.

[22] J. L. Rosa and P. Piçarra. "Existence and stability of relativistic fluid spheres supported by thin shells". *Physical Review D* 102.6 (Sept. 2020). DOI: 10.1103/physrevd.102.064009.

[23] G. Raposo et al. "Anisotropic stars as ultracompact objects in general relativity". *Physical Review D* 99.10 (May 2019). DOI: 10.1103/physrevd.99.104072.

[24] S.-C. Leung, M.-C. Chu, and L.-M. Lin. "Dark-matter admixed neutron stars". *Physical Review D* 84.10 (Nov. 2011). DOI: 10.1103/physrevd.84.107301.

[25] R. Abuter et al. (The GRAVITY Collaboration). "Detection of orbital motions near the last stable circular orbit of the massive black hole Sgr A*". *Astronomy & Astrophysics* 618 (Oct. 2018), p. L10. DOI: 10.1051/0004-6361/201834294.

[26] N. Scepi, J. Dexter, and M. C. Begelman. "Sgr A* X-ray flares from non-thermal particle acceleration in a magnetically arrested disc". *Monthly Notices of the Royal Astronomical Society* 511.3 (Feb. 2022), pp. 3536–3547. DOI: 10.1093/mnras/stac337.

[27] M. Bauböck et al. "Modeling the orbital motion of Sgr A*'s near-infrared flares". *Astronomy & Astrophysics* 635 (Mar. 2020), A143. DOI: 10.1051/0004-6361/201937233.

[28] J. L. Rosa et al. "Observational signatures of hot spots orbiting horizonless objects". *Physical Review D* 106.4 (Aug. 2022). DOI: 10.1103/physrevd.106.044031.

[29] F. H. Vincent et al. "GYOTO: a new general relativistic ray-tracing code". *Classical and Quantum Gravity* 28.22 (Oct. 2011), p. 225011. DOI: 10.1088/0264-9381/28/22/225011.

[30] E. Poisson. *A Relativist's Toolkit: The Mathematics of Black-Hole Mechanics*. Cambridge University Press, 2004. DOI: 10.1017/CBO9780511606601.

[31] S. M. Carroll. *Spacetime and Geometry: An Introduction to General Relativity*. Cambridge University Press, 2019. DOI: 10.1017/9781108770385.

[32] E. Berti. *Black Hole Perturbation Theory*. July 2016. URL: https://www.icts.res.in/event/page/3071.

[33] S. Chandrasekhar. “The Mathematical Theory of Black Holes”. In: *General Relativity and Gravitation: Invited Papers and Discussion Reports of the 10th International Conference on General Relativity and Gravitation, Padua, July 3–8, 1983*. Ed. by B. Bertotti, F. de Felice, and A. Pascolini. Dordrecht: Springer Netherlands, 1984, pp. 5–26. ISBN: 978-94-009-6469-3. DOI: 10.1007/978-94-009-6469-3_2.

[34] H. A. Buchdahl. “General Relativistic Fluid Spheres”. *Phys. Rev.* 116 (4 Nov. 1959), pp. 1027–1034. DOI: 10.1103/PhysRev.116.1027.

[35] V. Sopova and L. H. Ford. “Energy density in the Casimir effect”. *Physical Review D* 66.4 (Aug. 2002). DOI: 10.1103/physrevd.66.045026.

[36] P. V. Cunha, E. Berti, and C. A. Herdeiro. “Light-Ring Stability for Ultracompact Objects”. *Physical Review Letters* 119.25 (Dec. 2017). DOI: 10.1103/physrevlett.119.251102.

[37] J. L. Rosa. “Observational properties of relativistic fluid spheres with thin accretion disks”. *Physical Review D* 107.8 (Apr. 2023). DOI: 10.1103/physrevd.107.084048.

[38] C. F. B. Macedo et al. “Astrophysical signatures of boson stars: Quasinormal modes and inspiral resonances”. *Physical Review D* 88.6 (Sept. 2013). DOI: 10.1103/physrevd.88.064046.

[39] V. Cardoso et al. “ECO-spotting: looking for extremely compact objects with bosonic fields”. *Classical and Quantum Gravity* 39.3 (Jan. 2022), p. 034001. DOI: 10.1088/1361-6382/ac41e7.

[40] Fuerst, S. V. and Wu, K. “Radiation transfer of emission lines in curved space-time”. *A&A* 424.3 (2004), pp. 733–746. DOI: 10.1051/0004-6361:20035814.

[41] J. Dexter and E. Agol. “A fast new public code for computing photon orbits in a Kerr spacetime”. *The Astrophysical Journal* 696.2 (Apr. 2009), p. 1616. DOI: 10.1088/0004-637X/696/2/1616.

[42] N. Hamaus et al. “Prospects for testing the nature of Sgr A* near-infrared flares on the basis of current very large telescope - and future very large telescope interferometer - observations”. *The Astrophysical Journal* 692.1 (Feb. 2009), pp. 902–916. DOI: 10.1088/0004-637x/692/1/902.

A Code

A.1 GyotoThinShell.h

```
#ifndef __GyotoThinShell_H_
#define __GyotoThinShell_H_

#include <GyotoMetric.h>

namespace Gyoto {
  namespace Metric { class ThinShell; }
}

class Gyoto::Metric::ThinShell
: public Gyoto::Metric::Generic
{
  friend class Gyoto::SmartPointer<Gyoto::Metric::ThinShell>;

 protected:
  double par_ ;  // radius of the star
  double par2_; // radius of the shell

 private:

 public:
  void par(const double);
  void par2(const double);
  double par() const;
  double par2() const;

  GYOTO_OBJECT;
  ThinShell();
  virtual ThinShell* clone() const ;

  // metric components
  void gmunu(double g[4][4], const double x[4]) const ;
  // christoffel symbols
  int christoffel(double dst[4][4][4], const double x[4]) const ;
  // circular velocity
  virtual void circularVelocity(double const pos[4], double vel [4],
                                double dir=1.) const ;
};

#endif
```

A.2 ThinShell.C

```
#include "GyotoUtils.h"
#include "GyotoFactoryMessenger.h"
```

```
#include "GyotoThinShell.h"
#include "GyotoWorldline.h"
#include "GyotoError.h"
#include "GyotoProperty.h"
#include <cmath>

using namespace std ;
using namespace Gyoto ;
using namespace Gyoto::Metric ;

GYOTO_PROPERTY_START(ThinShell,
                     "Flat space-time.")
GYOTO_PROPERTY_DOUBLE(ThinShell, Par, par,
                      "Free parameter")     // radius of the star
GYOTO_PROPERTY_DOUBLE(ThinShell, Par2, par2,
                      "Free parameter 2")   // radius of the shell
                       ↪
GYOTO_PROPERTY_END(ThinShell, Generic::properties)

ThinShell::ThinShell() :
  Generic(GYOTO_COORDKIND_SPHERICAL, "ThinShell"),
  par_(1),
  par2_(1)
{}

// Mutators
void ThinShell::par(const double e) {
  par_=e;
  tellListeners();
}
void ThinShell::par2(const double e) {
  par2_=e;
  tellListeners();
}

// Accessors
double ThinShell::par() const { return par_ ; }
double ThinShell::par2() const { return par2_ ; }

void ThinShell::gmunu(double g[4][4], const double * pos) const
{
  GYOTO_DEBUG<<endl;
  size_t mu, nu;
  for (mu=0; mu<4; ++mu)
        for (nu=mu+1; nu<4; ++nu)
          g[mu][nu]=g[nu][mu]=0;
  double R = par_; // radius of the star
  double rs = par2_; // radius of the shell
  double rs2 = rs*rs;
```

```
  double r=pos[1];
  double sth2, cth2;
  sincos(pos[2], &sth2, &cth2);
  sth2*=sth2; cth2*=cth2;
  double r2=r*r;
  double R3 = R*R*R;

  // calculations for smooth transition
  double gtte = -1.+2./rs;
  double gtti = -1./4.*(3.*sqrt (1. - 2./R) - sqrt (1. -
   ↪  2.*rs2/(R3)))*(3.*sqrt (1. - 2./R) - sqrt (1. - 2.*rs2/(R3)));
  double a = gtte/gtti;

  double grri = 1/(1.-2.*rs2/R3);
  double grre = 1/(1. -2./rs);

  if (r > rs){ // Schwarzschild exterior
      for (mu=0; mu<4; ++mu){
              for (nu=0; nu<4; ++nu){
                              g[mu][nu]=g[nu][mu]=0;
                      }
    }
          g[0][0] = -1.+2./r;
          g[1][1] = 1./(1. -2./r);
          g[2][2] = r2;
          g[3][3] = r2*sth2;
  } else {// Schwarzschild interior
          for (mu=0; mu<4; ++mu){
           for (nu=0; nu<4; ++nu){
             g[mu][nu]=g[nu][mu]=0;
           }
    }
    g[0][0] = a*(-1./4.*(3.*sqrt (1. - 2./R) - sqrt (1. -
    ↪  2.*r2/(R3)))*(3.*sqrt (1. - 2./R) - sqrt (1. - 2.*r2/(R3))));
          g[1][1] = 1./(1.-2.*r2/R3);
          g[2][2] = r2;
          g[3][3] = r2*sth2;
  }

  GYOTO_DEBUG<<"done"<<endl;

}

int ThinShell::christoffel(double dst[4][4][4], const double pos[8]) const {
  GYOTO_DEBUG<<endl;
  size_t alpha, mu, nu;
  // fills metric with zeros
  for (alpha=0; alpha<4; ++alpha)
        for (mu=0; mu<4; ++mu)
```

```
        for (nu=0; nu<4; ++nu)
  dst[alpha][mu][nu]=0.;
double R = par_; // radius of the star
double rs = par2_; // radius of the shell
double rs2 = rs*rs;
double r=pos[1];
double sth, cth;
sincos(pos[2], &sth, &cth);
double sthcth = sth*cth;
double ctgth = cth/sth;
double sth2=sth*sth; double cth2 =cth*cth; // sin^2, cos^2
double r2=r*r;
double r3 = r2*r;
double R3 = R*R*R;

// calculations for smooth transition
double gtte = -1.+2./rs;
double gtti = -1./4.*(3.*sqrt (1. - 2./R) - sqrt (1. -
↪  2.*rs2/(R3)))*(3.*sqrt (1. - 2./R) - sqrt (1. - 2.*rs2/(R3)));
double a = gtte/gtti;

double grri = 1/(1.-2.*rs2/R3);
double grre = 1/(1. -2./rs);

if (r > rs){ // Schwarzschild exterior
      dst[0][0][1] = dst[0][1][0] = 1./(r2 - 2.*r);

    dst[1][0][0] = (-2.+r)/r3;
    dst[1][1][1] = 1./(2.*r - r2);
    dst[1][2][2] = 2.-r;
    dst[1][3][3] = (2. - r)*sth2;

    dst[2][1][2] = dst[2][2][1] = dst[3][1][3] = dst[3][3][1] = 1./r;
    dst[2][3][3] = -cth*sth;

    dst[3][2][3] = dst[3][3][2] = ctgth;
} else { // Schwarzschild interior
    dst[0][0][1] = dst[0][1][0] = 2.*r/(2.*r2+(-1.+3.*sqrt
     ↪  (1.-2.*r2/R3)*sqrt (1.-2./R))*R3);
    //dst[1][0][0] = r3/(R3*R3) + r*(-1.+3.*sqrt (1-2.*r2/R3)*sqrt
     ↪  (1.-2./R))/(2.*R3);
    dst[1][0][0] = (a*r*(-1.+3.*sqrt (1.-2.*r2/R3)*sqrt (1.-2./R) +
     ↪  2.*r2/R3))/(2.*R3);

    dst[1][1][1] = -2.*r/(2.*r2 - R3);
    dst[1][2][2] = (-r + 2.*r3/R3);
    dst[1][3][3] = (-r*(1.- 2.*r2/R3)*sth2);

    dst[2][1][2] = 1./r;
```

```
    dst[2][2][1] = 1./r;
    dst[2][3][3] = -sthcth;

    dst[3][1][3] = 1./r;
    dst[3][2][3] = ctgth;
    dst[3][3][1] = 1./r;
    dst[3][3][2] = ctgth;
  }
  return 0;
}

void ThinShell::circularVelocity(double const coor[4], double vel[4],
                              double dir) const {
  if (keplerian_) {
      Generic::circularVelocity(coor, vel, dir);
      return;
  }

# if GYOTO_DEBUG_ENABLED
  GYOTO_DEBUG<<"coor=["<<coor[0]<<", "<<coor[1]<<", "<<coor[2]<<",
   ↪  "<<coor[3]
             <<"], dir="<<dir<<endl;
# endif
  double sinth = sin(coor[2]);
  double coord[4] = {coor[0], coor[1]*sinth, M_PI*0.5, coor[3]};

  double rs = par2_; // radius of the shell
  double rs2 = rs*rs;
  double R = par_; // radius of the star
  double R3 = R*R*R;
  double r2 = coord[1]*coord[1];

  // calculations for smooth transitions of gtt
  double gtte = -1.+2./rs;
  double gtti = -1./4.*(3.*sqrt (1. - 2./R) - sqrt (1. -
   ↪  2.*rs2/(R3)))*(3.*sqrt (1. - 2./R) - sqrt (1. - 2.*rs2/(R3)));
  double a = gtte/gtti;

  vel[1] = vel[2] = 0.;
  if (coord[1] > rs) { // Scwharzschild exterior
      vel[3] = 1./((dir*pow(coord[1], 1.5))); // sqrt(1/r^3)
  }
  else { // Schwarzschild interior
      vel[3] = 1./2.*sqrt (a*(-2./R3 + (6.*sqrt (1.-2.*r2/R3)*sqrt
       ↪  ((-2.+R)/R))/(-2.*r2+R3)));
  }

  vel[0] = SysPrimeToTdot(coor, vel+1);
  vel[3] *= vel[0];
```

```
# if GYOTO_DEBUG_ENABLED
  GYOTO_DEBUG_ARRAY(vel,4);
# endif
}
```

A.3 interactive_hotspot.py

```
import numpy as np
import math
import matplotlib.pyplot as plt
import matplotlib.colors as colors
import gyoto
import gyoto.std
import gyoto.core
import sys
from astropy.io import fits
import time
import os

#gyoto.core.debug(True)

########################################
# TAKE INPUTS FOR THE REST OF THE CODE #
########################################

input_option = 1

if input_option == 1:

        choose_metric = 2           # 1. KerrBL; 2. ThinShell;
        spin_par = 0.               # KerrBL only
        star_par = 2.25             # ThinShell only
        shell_par = 2.5             # ThinShell only
        metric_mass = 4.26e6        # Sgr A* = 4.26e6 sunmass

        obs_angle = 80              # In degrees
        time_steps = 200
        resolution = 2000           # In pixels
        obs_distance = 1000         # In units of M
        field_view = 200            # In micro arcseconds
        screen_dist = 8.25          # Srg A* = 8.25 kiloparsec

        object_type = 2             # 1. Equatorial hot-spot; 2. Isotropic
         ↪  star
        object_radius = 0.5         # Radius of the hot spot
        orbit_radius = 8            # Hot spot orbit radius
        object_thin = True          # Optically thin
```

```
        want_mask = True
        see_mask = True
        mask_radius = 1.            # Times the radius of the object

        trace_rays = False
        number_rays = 180           # Number of positions in the orbit
        tracing_type = 2            # 1. Full image; 2. Single pixel
        see_images = False          # Full image only
        save_images = False         # Full image only
        produce_fits = False        # Full image only
        x_pixel = 25                # Single pixel only
        y_pixel = 32                # Single pixel only

        plot_geodesic = False
        congr_z = 734
        no_of_track = 1             # Geodesic only, no of track starting
         ↪  from outside
        geod_x = 1000               # Geodesic only
        geod_y =  1265              # Geodesic only
        xy_plot = False             # Geodesic only
        yz_plot = True              # Geodesic only
        show_yz = True
        rz_plot = False             # Geodesic only

        astrometry = False
        show_astrometry = False
        fits_file = "st5sh5_res500_angle50_d8.fits"
        centroid = False
        magnitude = False
        int_flux = True


################################
# Select metric and properties #
################################

if choose_metric == 1: #Kerr black-hole
        metric = gyoto.std.KerrBL()
        metric.spin(spin_par)

if choose_metric == 2: #Piecewise
        gyoto.core.loadPlugin('null')
        metric = gyoto.core.Metric('ThinShell')
        metric.set('Par', star_par) # radius of the star
        metric.set('Par2', shell_par) # radius of the shell

metric.mass(metric_mass,"sunmass")

##############################
```

```
# Observation specifications #
##############################

obs_theta_deg = obs_angle   # Observation angle in degrees
nt = time_steps                 # Time steps in light curve
Npix = resolution               # Image size in pixels N x N
length = obs_distance           # Times and distances

obs_theta = obs_theta_deg*math.pi/180.
obs_time = length
obs_radius = length
obs_phi = 0

obs_position=np.asarray([obs_time,obs_radius,obs_theta,obs_phi])

#####################################
# Select observer screen parameters #
#####################################

fov = field_view
sgrdist = screen_dist

screen = gyoto.Screen()

#screen.setObserverPos(obs_position)
screen.metric(metric)
screen.distance(sgrdist,"kpc")
screen.time(sgrdist,"kpc")
screen.fieldOfView(fov,"µas")              #Default is radians
screen.inclination(np.pi-obs_theta)
screen.PALN(180.,"°")
screen.resolution(Npix)



###############################
# Define astrophysical object #
###############################

obj_size = object_radius

if object_type == 1: #equatorial hot spot
    equat = gyoto.std.EquatorialHotSpot()
    equat.spotRadSize(obj_size)
    equat.beaming("IsotropicBeaming")

if object_type == 2: #star
    equat = gyoto.std.Star()
    equat.radius(obj_size)
```

```
    equat.isotropic(True)


equat.metric(metric)
equat.rMax(50.)
equat.opticallyThin(object_thin)



#############################
# Define orbital properties #
#############################

equat_timeinit = length
equat_orbitradius = orbit_radius
equat_theta = math.pi/2.
equat_phi = 0.

equat_position = np.asarray([equat_timeinit, equat_orbitradius, equat_theta,
 ↪  equat_phi])
equat.setPosition(equat_position)

circular_velocity = 0 * equat_position
metric.circularVelocity(equat_position,circular_velocity, 1.0)

equat_drdt = 0.
equat_dthetadt = 0.
equat_dphidt = circular_velocity[3]/circular_velocity[0]
equat_orbitalperiod = 2*np.pi/equat_dphidt

equat_velocity=np.asarray([equat_drdt,equat_dthetadt,equat_dphidt])
equat.setVelocity(equat_velocity)



###############################
# Unit conversions to minutes #
###############################

kpc2m = 3.08568025e19 #kpc in meter
c_SI = 299792458. #c in SI
kpc2min = kpc2m/c_SI/60 # convert kpc to minutes
screen_dist_min = screen_dist * kpc2min #distance in minutes

G_SI = 6.67428e-11 #gravitational constant in SI
sun_mass_SI = 1.98843e30 #solar mass in SI
geometric2min = G_SI*metric_mass*sun_mass_SI/c_SI**3/60 #geometric time to
 ↪  minutes
```

```
period_min = equat_orbitalperiod * geometric2min



##############################
# Define Scenery properties #
##############################

sceneryEquat = gyoto.Scenery()
sceneryEquat.metric(metric)
sceneryEquat.screen(screen)
sceneryEquat.astrobj(equat)
sceneryEquat.tMin(-1000.)
sceneryEquat.nThreads(1)
sceneryEquat.requestedQuantitiesString('Intensity')



###############
# Define Mask #
###############

if(want_mask): # Chose if you want a mask
        scclone = sceneryEquat.clone()

        tr = gyoto.std.StarTrace()
        tr.radius(mask_radius*equat.radius())
        tr.metric(equat.metric())
        coord = equat.initCoord()
        tr.initCoord(coord)
        tr.opticallyThin(object_thin)
        tr.TMin(0)
        tr.TMax(equat_orbitalperiod)
        tr.delta(tr.radius())
        tr.adaptive(False)

        #print(tr.getProperties())

        scclone.astrobj(tr)
        scclone.requestedQuantitiesString("Intensity")

        print("Computing mask...")

        intensity = scclone.rayTrace()['Intensity'] # Add (yy,xx) to get for
         ↪  a particular pixel
        mask = np.double(intensity>0)
        mask_array = gyoto.core.array_double.fromnumpy2(mask)

        sceneryEquat.screen().mask(mask_array, Npix)
```

```
        if(see_mask): #Chose if you want to see the mask
            plt.figure(1)
            plt.imshow(intensity)
            plt.show()



################
# Ray-tracing #
################

if trace_rays:

        all_data = np.empty([number_rays, Npix, Npix])

        for i in range(number_rays):

            # Use these two lines instead of the following two to rotate the
             ↪  observer instead of the object
            #equat_phi = 2 * np.pi / number_rays * i
            #equat_position = np.asarray([equat_timeinit, equat_orbitradius,
             ↪  equat_theta, equat_phi])

            obs_time = screen_dist_min + i / number_rays * period_min
            screen.time(obs_time,"min")

            equat.setPosition(equat_position)
            equat.setVelocity(equat_velocity)

            # Ray trace the whole image

            if tracing_type == 1:

                image = sceneryEquat.rayTrace()['Intensity']
                all_data[i,:,:] = image

                plt.figure(2)
                plt.imshow(image)


                if see_images:

                    plt.show()

                if save_images:

                    path = f"img/image_{i}"
                    plt.savefig(path)
```

```
                print(f"Image number {i+1} saved...")


            # Ray trace a single pixel

            if tracing_type == 2:

                xx = x_pixel
                yy = y_pixel


                flux = sceneryEquat.rayTrace(yy, xx)['Intensity']
                print ('flux of pixel (',xx,',',yy,') =', flux)

        if produce_fits:

            hdr = fits.Header()
            hdu = fits.PrimaryHDU(all_data, header=hdr)
            hdu.writeto(fits_file)



#######################
# Trace the geodesics #
#######################

if plot_geodesic:

        dest = np.zeros(8, float)
        sceneryEquat.screen().getRayCoord(geod_x+1,geod_y+1,dest)
        ph = gyoto.core.Photon()
        ph.setInitialCondition(sceneryEquat.metric(),
         ↪  sceneryEquat.astrobj(), dest)
        aop=gyoto.core.AstrobjProperties()
        ph.spectrometer(sceneryEquat.screen().spectrometer())
        ph.deltaMaxOverR(0.1)

        ph.hit(aop)

        nn=ph.get_nelements()
        tt=np.ndarray(nn)
        rBL=np.ndarray(nn)
        theta=np.ndarray(nn)
        phi=np.ndarray(nn)
        ph.get_t(tt)
        ph.getCoord(tt, rBL, theta, phi)

        xpl1 = rBL * np.sin(theta) * np.cos(phi)
```

```
ypl1 = rBL * np.sin(theta) * np.sin(phi)
zpl1 = rBL * np.cos(theta)
rcyl1 = rBL * np.sin(theta)

xcirc=np.arange(-orbit_radius,orbit_radius+.1,0.1)
ycirc1=(orbit_radius ** 2-xcirc ** 2) ** (1/2)
ycirc2=-(orbit_radius ** 2-xcirc ** 2) ** (1/2)

xcirch=np.arange(-2,2.1,0.1)
ycirc1h=(4-xcirch ** 2) ** (1/2)
ycirc2h=-(4-xcirch ** 2) ** (1/2)

print("Saving the geodesics of",congr_z,"...")
data_folder = ""
for l in fits_file:
    if l == "_":
        break
    data_folder += l
data_path_geod =
 ↪  "/home/hanna/Gyoto/plugins/null/lib/data/"+data_folder+"/geod_data_congr"
# creates directory if it doesn't exist already
isExist = os.path.exists(data_path_geod)
if not isExist:
    os.makedirs(data_path_geod)
xy_pdf_filename = os.path.join(data_path_geod,
 ↪  fits_file[:-5:]+"_tr_"+str(no_of_track)+"_xy.pdf")
yz_pdf_filename = os.path.join(data_path_geod,
 ↪  fits_file[:-5:]+"_tr_"+str(no_of_track)+"_yz.pdf")
rz_pdf_filename = os.path.join(data_path_geod,
 ↪  fits_file[:-5:]+"_tr"+str(no_of_track)+"_rz.pdf")

xy_txt_filename = os.path.join(data_path_geod,
 ↪  fits_file[:-5:]+"_tr_"+str(no_of_track)+"_xy.txt")
yz_txt_filename = os.path.join(data_path_geod,
 ↪  fits_file[:-5:]+"_tr_"+str(no_of_track)+"_yz.txt")
rz_txt_filename = os.path.join(data_path_geod,
 ↪  fits_file[:-5:]+"_tr"+str(no_of_track)+"_rz.txt")

if xy_plot:

    plt.figure(3)
    plt.plot(xpl1, ypl1, color="red", linestyle='solid',
     ↪  linewidth=2)
    #plt.plot(xpl2, ypl2, color="blue", linestyle='solid',
     ↪  linewidth=2)
    plt.plot(xcirc, ycirc1, color="black", linestyle='dashed',
     ↪  linewidth=2)
    plt.plot(xcirc, ycirc2, color="black", linestyle='dashed',
     ↪  linewidth=2)
```

```
    plt.xlim(-10.,10.)
    plt.ylim(-10.,10.)
    plt.xticks(fontsize=14)
    plt.yticks(fontsize=14)
    plt.xlabel(”x (M)”, fontsize=14)
    plt.ylabel(”y (M)”, fontsize=14)
    plt.savefig(xy_pdf_filename,bbox_inches=”tight”)
    plt.show()


if yz_plot:

    plt.figure(4)
    plt.plot(ypl1, zpl1, color=”red”, linestyle='solid',
     ↪  linewidth=2)
    #plt.plot(ypl2, zpl2, color=”blue”, linestyle='solid',
     ↪  linewidth=2)
    plt.plot(xcirch, ycirc1h, color=”black”, linestyle='dashed',
     ↪  linewidth=2)
    plt.plot(xcirch, ycirc2h, color=”black”, linestyle='dashed',
     ↪  linewidth=2)
    plt.xlim(-10.,10.)
    plt.ylim(-10.,10.)
    plt.xticks(fontsize=14)
    plt.yticks(fontsize=14)
    plt.xlabel(”y (M)”, fontsize=14)
    plt.ylabel(”z (M)”, fontsize=14)
    #plt.savefig(yz_pdf_filename,bbox_inches=”tight”)
    if show_yz:
        plt.show()

    file = open(yz_txt_filename, ”w”)
    file.write(”y\tz\n”)
    for y, z in zip(ypl1, zpl1):
        file.write(str(y)+”\t”+str(z)+”\n”)
    file.close()
    print(”Finished!”)

if rz_plot:

    plt.figure(5)
    plt.plot(rcyl1, zpl1, color=”red”, linestyle='solid',
     ↪  linewidth=2)
    #plt.plot(rcyl2, zpl2, color=”blue”, linestyle='solid',
     ↪  linewidth=2)
    plt.plot(xcirch, ycirc1h, color=”black”, linestyle='dashed',
     ↪  linewidth=2)
    plt.plot(xcirch, ycirc2h, color=”black”, linestyle='dashed',
     ↪  linewidth=2)
```

```
            plt.xlim(-10.,30.)
            plt.ylim(-30.,30.)
            plt.xticks(fontsize=14)
            plt.yticks(fontsize=14)
            plt.xlabel("r (M)", fontsize=14)
            plt.ylabel("z (M)", fontsize=14)
            plt.savefig(rz_pdf_filename,bbox_inches="tight")
            plt.show()



########################
# Astrometric analysis #
########################

if astrometry:

        hdu = fits.open(fits_file)
        cube = hdu[0].data
        hdu.close()

        n_time = cube.shape[0]
        n_pix = cube.shape[1]
        period = np.linspace(0, 1, n_time)

        grid = np.mgrid[0:n_pix, 0:n_pix]
        xx = grid[1, :, :]
        yy = grid[0, :, :]

        xx = np.concatenate([xx[np.newaxis, :, :]]*n_time)
        yy = np.concatenate([yy[np.newaxis, :, :]]*n_time)

        cube_sum =  np.sum(cube, axis = tuple([1,2]))
#   print("max=", np.max(cube_sum), "min=", np.min(cube_sum))

        cube_x = np.sum(cube * xx, axis = tuple([1,2]))
        cube_x /= cube_sum

        cube_y = np.sum(cube * yy, axis = tuple([1,2]))
        cube_y /= cube_sum

        result = np.concatenate([cube_x[np.newaxis, :]]*3)
        result[0, :] = cube_x
        result[1, :] = cube_y
        result[2, :] = cube_sum

        zero_p = np.where(cube_sum == np.min(cube_sum))[0][0]
        result = np.roll(result, -zero_p, axis=1)
```

```
data_folder = ""
for l in fits_file:
    if l == "_":
        break
    data_folder += l
data_path = "/home/hanna/Gyoto/plugins/null/lib/data/"+data_folder
# create directory
isExist = os.path.exists(data_path)
if not isExist:
    os.makedirs(data_path)
filename = os.path.join(data_path, fits_file[:-5:]+".txt")
int_filename = os.path.join(data_path, fits_file[:-5:]+".pdf")
int_textfilename = os.path.join(data_path,
↪  fits_file[:-5:]+"_int.txt")

if magnitude:

    flux = result[2,:]
    total_mag = - 2.5 * np.log10(flux / np.amin(flux))

    plt.figure(6)
    plt.plot(period, -total_mag, color="red", linestyle='solid',
     ↪  linewidth=2)
    plt.xlim(0.,1.)
    plt.ylim(0.,6.)
    plt.xticks(fontsize=14)
    plt.yticks(fontsize=14)
    plt.xlabel("time (t/T)", fontsize=14)
    plt.ylabel("magnitude", fontsize=14)
    if show_astrometry:
        plt.show()


if centroid:

    if obs_angle == 90:

        xt = result[0,:]

        plt.figure(7)
        plt.plot((xt - n_pix / 2) * field_view / n_pix, period * 200
         ↪  - 100, color="red", linestyle='solid', linewidth=2)
        plt.xlim(-field_view / 2 , field_view / 2)
        plt.ylim(0,100)
        plt.xticks(fontsize=14)
        plt.yticks(fontsize=14)
        plt.xlabel("x_centroid", fontsize=14)
        plt.ylabel("time", fontsize=14)
        if show_astrometry:
```

```
                plt.show()

        else:

            plt.figure(7)
            centroid_x = (result[0,:] - n_pix / 2) * field_view / n_pix
            centroid_y = (result[1,:] - n_pix / 2) * field_view / n_pix
            plt.plot(centroid_x,
                     centroid_y,
                     color="red", linestyle='solid', linewidth=2)
            plt.xlim(-field_view / 2 , field_view / 2)
            plt.ylim(-field_view / 2 , field_view / 2)
            plt.xticks(fontsize=14)
            plt.yticks(fontsize=14)
            plt.xlabel("x_centroid", fontsize=14)
            plt.ylabel("y_centroid", fontsize=14)
            if show_astrometry:
                plt.show()

    if int_flux:

        integrated = np.sum(cube,axis=0)
        #print(integrated)

        plt.figure(8)
        ext = 125
        plt.imshow(integrated,origin="lower",
         ↪  extent=[-ext,ext,-ext,ext],
                       norm=colors.PowerNorm(gamma=0.6,
                       vmin=0, vmax=10), cmap='inferno') #'YlGnBu'
        plt.xticks(fontsize=14)
        plt.yticks(fontsize=14)
        plt.xlabel("x", fontsize=14)
        plt.ylabel("y", fontsize=14)
        plt.savefig(int_filename,bbox_inches="tight")
        if show_astrometry:
            plt.show()

    file = open(filename, "w")
    file.write("Magnitude\tTime\n")
    for m, t in zip(-total_mag, period):
        file.write(str(m)+"\t"+str(t)+"\n")
    file.write("\nx_centroid\ty_centroid\n")
    for x, y in zip(centroid_x, centroid_y):
        file.write(str(x)+"\t"+str(y)+"\n")
    file.close()

    file2 = open(int_textfilename, "w")
    for line in integrated:
```

```
        for element in line:
            elToWrite = str(element)+"\t"
            file2.write(elToWrite)
        file2.write("\n")
    file2.close()
```

B Integrated flux

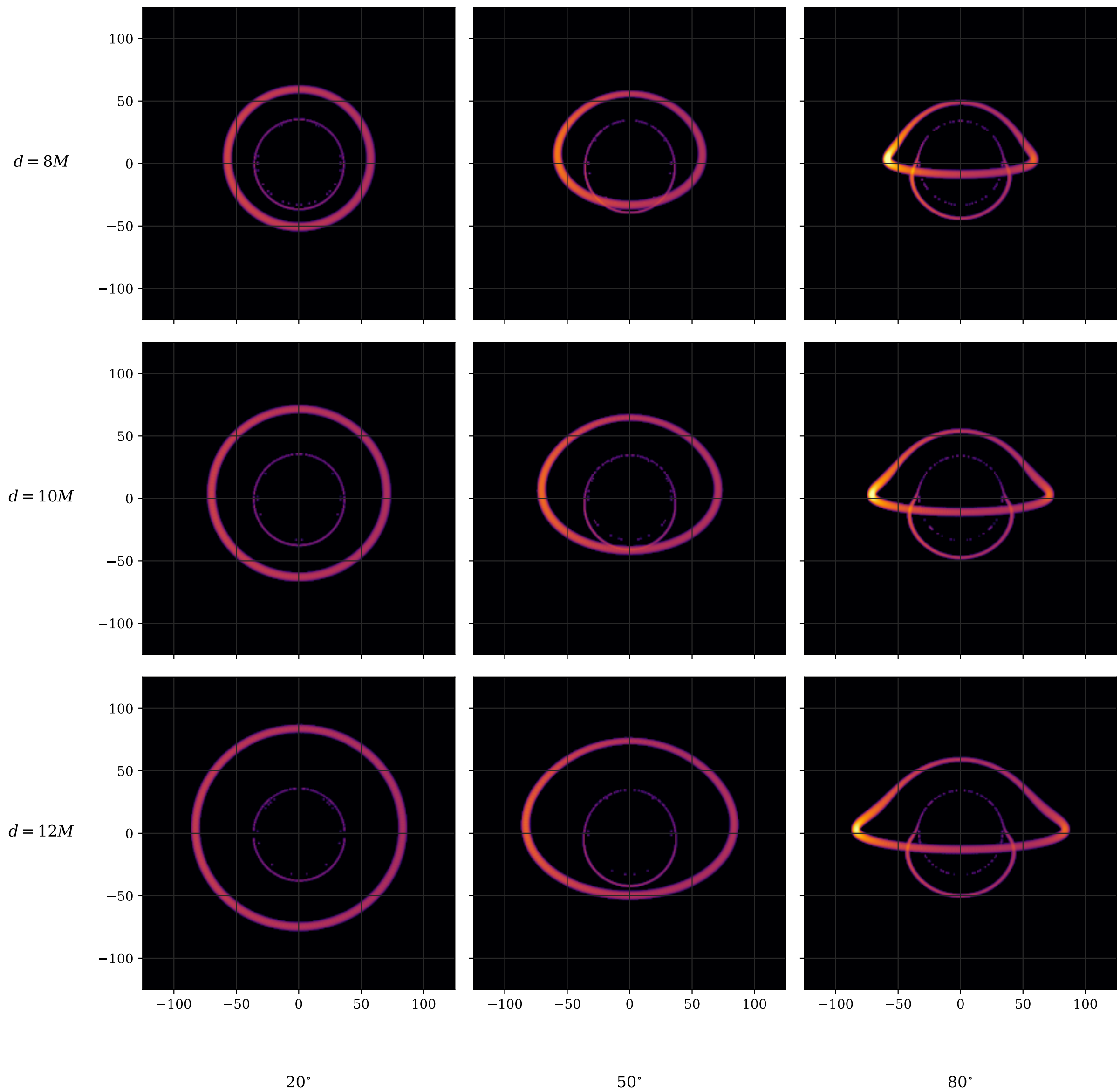

Figure 15. The integrated flux of the model $R = R_s = 2.25M$ for orbital radii $d \in \{8M, 10M, 12M\}$ (increasing from top to bottom) and inclination angles $i = 20°, 50°, 80°$ (increasing from left to right). The x- and y-axis are in units μas. The model resembles a Schwarzschild BH.

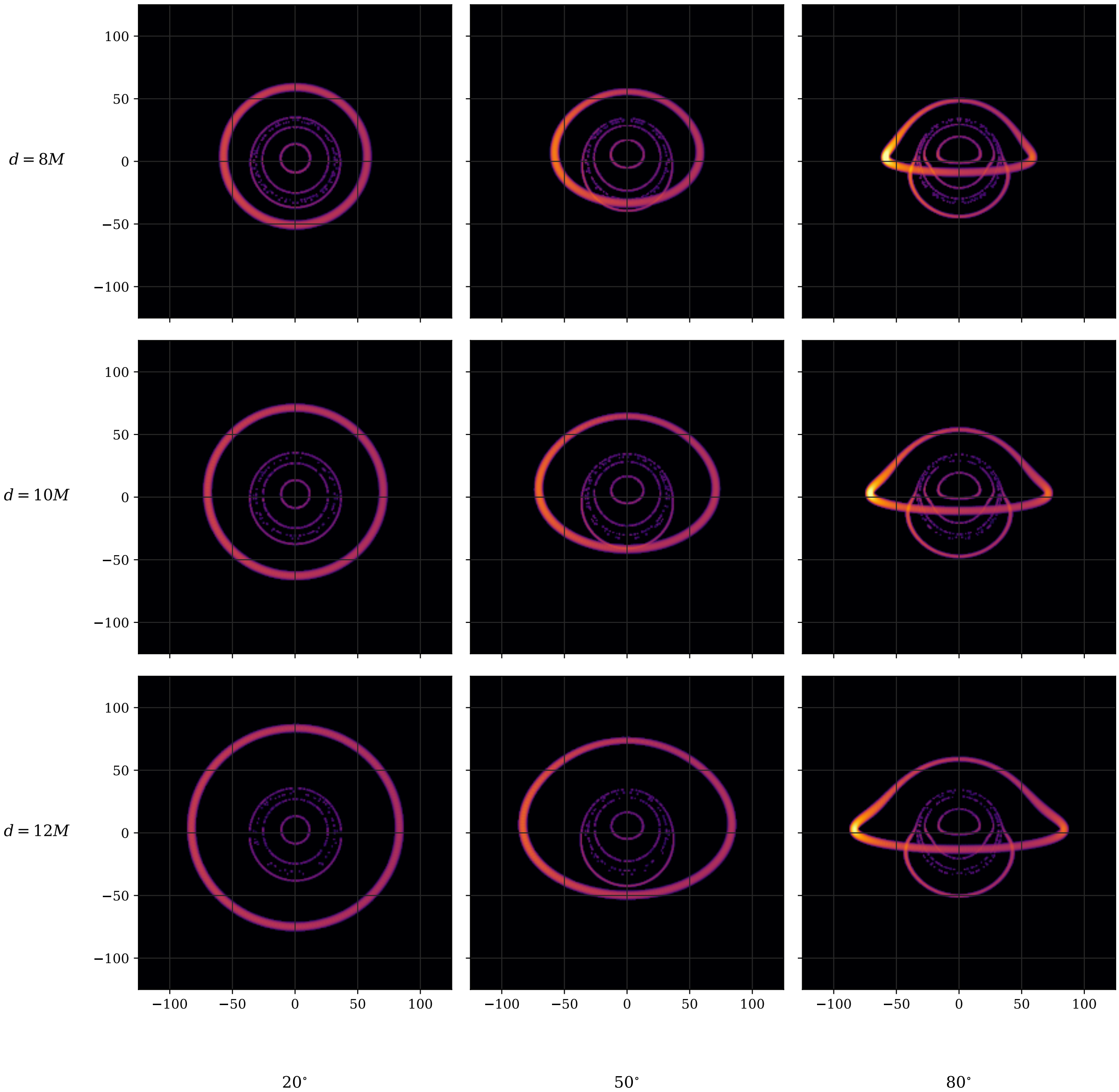

Figure 16. The integrated flux of the model $R = R_s = 2.5M$ for orbital radii $d \in \{8M, 10M, 12M\}$ (increasing from top to bottom) and inclination angles $i = 20°, 50°, 80°$ (increasing from left to right). The x- and y-axis are in units μas. In addition to the usual Schwarzschild BH components, novel trajectories appear in the interior.

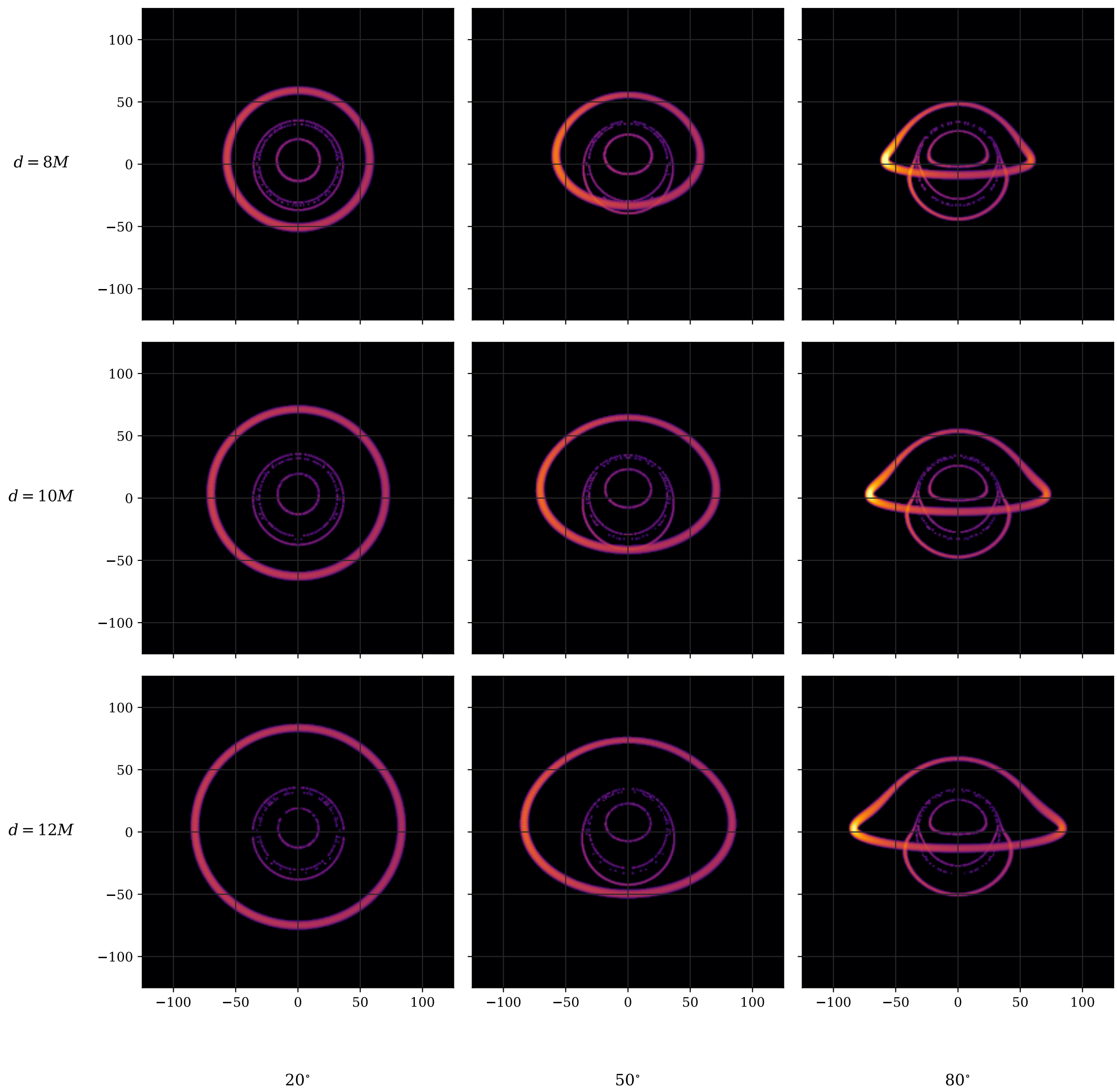

Figure 17. The integrated flux of the model $R = R_s = 3M$ for orbital radii $d \in \{8M, 10M, 12M\}$ (increasing from top to bottom) and inclination angles $i = 20°, 50°, 80°$ (increasing from left to right). The x- and y-axis are in units μas. In addition to the usual Schwarzschild BH components, novel trajectories appear in the interior.

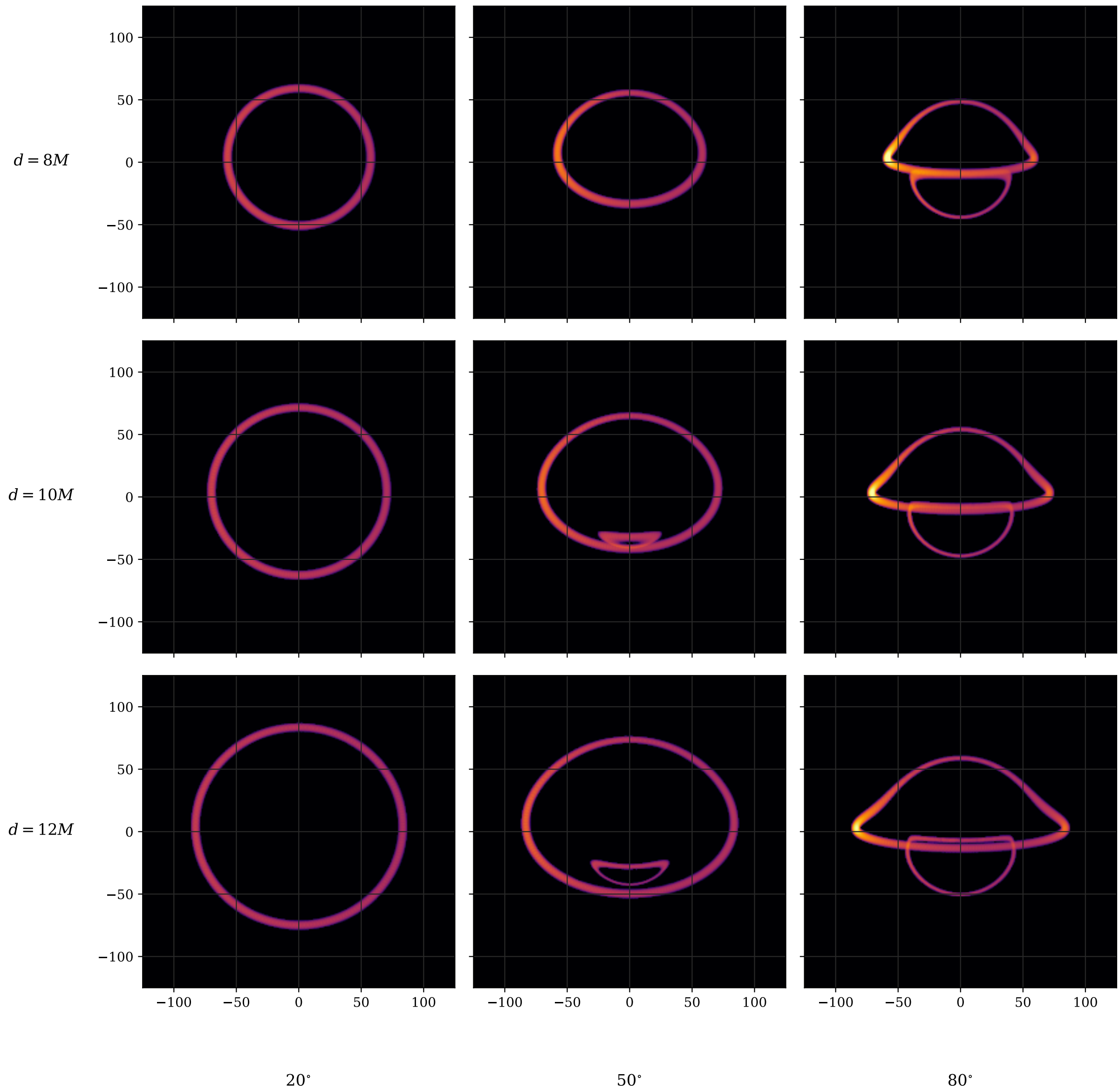

Figure 18. The integrated flux of the model $R = R_s = 5M$ The integrated flux of the model $R = R_s = 2.5M$ for orbital radii $d \in \{8M, 10M, 12M\}$ (increasing from top to bottom) and inclination angles $i = 20°, 50°, 80°$ (increasing from left to right). The x- and y-axis are in units μas. The model resembles a BS with a melded secondary track and plunge-through track.

Non-exclusive licence to reproduce the thesis and make the thesis public

I, **Hanna Liis Tamm**,

1. herewith grant the University of Tartu a free permit (non-exclusive licence) to

   reproduce, for the purpose of preservation, including for adding to the DSpace digital archives until the expiry of the term of copyright,

   OBSERVATIONAL PROPERTIES OF HOT SPOTS AROUND RELATIVISTIC FLUID SPHERES,

   supervised by João Luís Rosa, PhD and Laur Järv, PhD.

2. I grant the University of Tartu a permit to make the work specified in p. 1 available to the public via the web environment of the University of Tartu, including via the DSpace digital archives, under the Creative Commons licence CC BY NC ND 3.0, which allows, by giving appropriate credit to the author, to reproduce, distribute the work and communicate it to the public, and prohibits the creation of derivative works and any commercial use of the work until the expiry of the term of copyright.

3. I am aware of the fact that the author retains the rights specified in p. 1 and 2.

4. I certify that granting the non-exclusive licence does not infringe other persons' intellectual property rights or rights arising from the personal data protection legislation.

Hanna Liis Tamm
26/05/2023